

Scalable evaluation of incoherent infidelity in quantum devices

Jader P. Santos, I. Henao, and Raam Uzdin*

*Fritz Haber Research Center for Molecular Dynamics, Institute of Chemistry,
The Hebrew University of Jerusalem, Jerusalem 9190401, Israel*

Quantum processors can already execute tasks beyond the reach of classical simulation, albeit for artificial problems. At this point, it is essential to design error metrics that test the experimental accuracy of quantum algorithms with potential for a practical quantum advantage. The distinction between coherent errors and incoherent errors is crucial, as they often involve different error suppression tools. The first class encompasses miscalibrations of control signals and crosstalk, while the latter is usually related to stochastic events and unwanted interactions with the environment. We introduce the incoherent infidelity as a measure of incoherent errors and present a scalable method for measuring it. This method is applicable to generic quantum evolutions subjected to time-dependent Markovian noise. Moreover, it provides an error quantifier for the target circuit, rather than an error averaged over many circuits or quantum gates. The estimation of the incoherent infidelity is suitable to assess circuits with sufficiently low error rates, regardless of the circuit size, which is a natural requirement to run useful computations.

I. INTRODUCTION

The premise of quantum technology and quantum computing is to provide a dramatic improvement over classical devices. In particular, quantum computers and simulators aim to solve computational problems that would otherwise require unrealistic resources. Reliability is a key factor for the success of these devices. External noise and inaccuracies in the control signals that execute the computation presently limit the observation of a practical quantum advantage. Furthermore, the intricate nature of quantum evolution makes error detection and diagnostics very challenging. As a result of this complexity, error diagnostic methods such as (linear) cross entropy [1, 2] and quantum volume [3], which rely on classical simulations of the quantum evolution, are not scalable. Experimentally, it is known that although some special states admit a tomographic reconstruction with polynomial resources [4, 5], the tomographic cost is exponential in general [6] (even using advanced tomographic techniques like compressed sensing [7]). These experimental and computational hurdles have spurred the development of more efficient benchmarking approaches [8–13].

The majority of benchmarking techniques for quantum systems have been designed to assess the overall performance of a quantum device [14–16]. This includes randomized benchmarking (RB) and many of its variants [8–10, 17–24], as well as quantum volume [3]. In this holistic approach, which henceforth we will term “device benchmarking”, the purpose is to quantify the expected performance of a typical circuit executed on the benchmarked device. For example, RB protocols provide a single number that under some conditions is associated with the average gate infidelity. Device benchmarking methods can be very useful to study the average behavior of quantum processors and compare different quantum computing architectures. These methods are usually based on protocols that involve random quantum circuits, and therefore they may fail to predict the quality of specific quantum circuits. In particular, it has been noted that error metrics that exploit random quantum circuits cannot correctly characterize the performance of structured quantum algorithms [25].

The accurate assessment of quantum circuits is also hindered by the variety and complexity of errors that take place in quantum computers. Coherent errors and incoherent errors constitute two broad categories that occupy a special place in the theory of benchmarking. Coherent errors represent unitary deviations from the ideal evolution that a quantum device is instructed to execute. On the other hand, incoherent (or stochastic) errors arise from the interaction between the system and the environment, or due to random fluctuations in the control signals. Coherent errors are known to have a significant impact in NISQ (noisy intermediate scale quantum) devices [26–28]. Typical sources for these errors include defective calibration of quantum gates, or parasitic crosstalk terms like the $Z \otimes Z$ interaction between superconducting qubits [29, 30]. Yet, the theoretical framework of benchmarking often relies on the assumption of stochastic Pauli channels [31], which describe purely stochastic noise. While these channels can be engineered via randomized compiling (RC) [32], this introduces a potential noise overhead and the resulting randomized circuit may not reflect the performance of the target circuit being benchmarked. Moreover, RC operations are applied only on Clifford gates and errors affecting non-Clifford gates are neglected.

In this work, we introduce a method for assessing the quality of a quantum computation, executed by a target

quantum circuit, under the assumption of time-dependent Markovian noise. For a given input state, we consider the infidelity between the corresponding output state and its error-free counterpart. More precisely, our method is useful to measure a contribution to the infidelity that is exclusively associated with incoherent noise, which we term “incoherent infidelity”. Since the evaluation of this quantity does not involve any randomization of the target evolution, it provides a faithful measure of the strength of stochastic errors in an arbitrary target circuit.

As compared to device benchmarking, error diagnostics of target circuits is a less studied topic [34–38]. In particular, Interleaved RB [34] is a RB variant that can be applied to individual Clifford circuits, but it lacks scalability guarantees. Another benchmarking protocol termed Channel Spectrum Benchmarking [38] can in principle be employed for arbitrary target circuits. However, it requires knowing the eigendecomposition of the ideal (unitary) circuit to be evaluated, which may be prohibitive for many interesting cases. Cycle benchmarking (CB) [11] and Cycle Error Reconstruction [37] have been used to characterize shallow portions of a quantum circuit, known as “cycles”. More precisely, these methods benchmark “effective dressed cycles”, that result from the application of RC to the original cycle. Later on, an extension of Cycle Error Reconstruction was proposed for estimating coherent and incoherent error contributions in cycles [39]. Although these tools characterize the performance of single circuits (or cycles), it is worth mentioning that in all the cases the error metric is an average over a set of input states. Since this averaging seems to be an integral part of the underlying protocols, it is also unclear if they can be adapted to benchmark circuit performance for fixed initial states.

More recently, a method [36] using mirror circuits [25] was proposed to efficiently estimate the infidelity of arbitrary quantum circuits in a regime of sufficiently low error rates. This technique isolates the total circuit infidelity (including coherent and incoherent errors) from state preparation and measurement (SPAM) errors, and provides an average of this quantity over initial states. The method developed here is also robust to SPAM errors of moderate magnitude and is applicable to circuits with low infidelities. However, it can extract the incoherent infidelity associated with a fixed initial state or as an average over a set of input states, thereby providing additional flexibility to the benchmarking task. Furthermore, it admits an efficient implementation with computational and experimental resources that are independent of the size of the system.

This article is structured as follows. In Sec. II, we describe the basics of quantum mechanics in Liouville space [40], which is the framework used in our derivations. In Sec. III, we characterize the incoherent infidelity by using a generic master equation that clearly separates the dynamical contributions of coherent and incoherent errors. In Sec. IV, we introduce our method for estimating the incoherent infidelity. This method is based on the implementation of circuit sequences that alternate the target evolution with a proper implementation of its inverse. In Sec. V, we present numerical examples that illustrate the applicability of our technique in different situations. This involves circuits subjected to noise, coherent errors, and SPAM errors. In Sec. VI, we provide sufficient conditions for the scalability of our method, and we present the conclusions in Sec. VII.

II. PRELIMINARIES AND NOTATIONS

In the following, $H(t)$ will denote a time-dependent Hamiltonian and the time derivative will be written as d_t . For the derivation of our main results it will be useful to move from Hilbert space to Liouville space. In Liouville space, a density matrix ρ of dimension $N \times N$ is flattened into a column “density vector” of length N^2 . This vector can be expressed using a double ket notation, i.e. as $|\rho\rangle\rangle$. As a result, the Liouville von Neumann equation for unitary dynamics $id_t\rho = [H(t), \rho]$ becomes [40]:

$$id_t|\rho\rangle\rangle = H_L(t)|\rho\rangle\rangle, \quad (1)$$

$$H_L(t) = H(t) \otimes I - I \otimes H(t)^T, \quad (2)$$

where I is the identity operator in the original Hilbert space (the $N \times N$ identity matrix) and $H_L(t)$ is the Hamiltonian in Liouville space. Moreover, the superscript T denotes transposition.

Since $H_L(t)$ is hermitian, the resulting evolution operator in Liouville space at time t , denoted by $U_L(t)$, is unitary. That is, $U_L(t)U_L^\dagger(t) = I_L$, where I_L is the $N^2 \times N^2$ identity matrix. Due to the Schrödinger-like structure of Eq. (1), the solution to $|\rho\rangle\rangle$ takes the simple form $|\rho\rangle\rangle = U_L(t)|\rho_0\rangle\rangle$, even if the initial state ρ_0 is mixed. If the system is open and the dynamics is Markovian, the Schrödinger-like form 1 still holds and reads

$$d_t|\rho\rangle\rangle = (-iH_L(t) + \mathcal{L}(t))|\rho\rangle\rangle, \quad (3)$$

where $\mathcal{L}(t)$ is an operator hereafter called “dissipator”. This operator can also be time dependent and characterizes the non-unitary contribution to the evolution. When the evolution is described by a Lindblad master equation in

Hilbert space, it is straightforward to obtain $\mathcal{L}(t)$. However, the main results of this paper are independent of the explicit form of $\mathcal{L}(t)$. In particular, we also include dissipators that do not follow the Lindblad form, and thus are not associated with CPTP maps. Consequently, our method can quantify infidelity due to probability leakage to an inaccessible part of the Hilbert space.

Finally, the standard scalar product between two matrices A and B , given by $\text{Tr}[A^\dagger B]$ in Hilbert space, reads $\langle\langle A|B\rangle\rangle$ in Liouville space. Here, $|B\rangle\rangle$ is the Liouville space vector corresponding to B , and $\langle\langle A = |A\rangle\rangle^\dagger$. Accordingly, the expectation value of an operator A takes the form

$$\langle A \rangle = \text{Tr}[A^\dagger \rho] = \langle\langle A|\rho\rangle\rangle. \quad (4)$$

III. INCOHERENT INFIDELITY

In this section, we introduce and motivate the basic expression for the incoherent infidelity used in our framework. For simplicity, from now on we will refer to incoherent errors as “noise”. The effect of coherent errors can be characterized by introducing a Hamiltonian contribution $\delta H_L(t)$ to the dynamical equation (3). The resulting equation reads

$$\begin{aligned} d_t|\rho\rangle\rangle &= (-iH_L(t) - i\delta H_L(t) + \mathcal{L}(t))|\rho\rangle\rangle \\ &= (-iH_L(t) + \mathcal{L}'(t))|\rho\rangle\rangle, \end{aligned} \quad (5)$$

where $\mathcal{L}'(t) = -i\delta H_L(t) + \mathcal{L}(t)$. By convention, the dissipator $\mathcal{L}(t)$ represents pure noise in (5), and the perfect implementation of the target circuit is generated by the driving $H_L(t)$. Thus, any Hamiltonian deviation from $H_L(t)$ is absorbed into $\delta H_L(t)$. Note however that we do not need to specify the form of $\mathcal{L}(t)$, for the definition of the incoherent infidelity or for our derivations.

Let T be the total evolution time and \tilde{K} the evolution operator that corresponds to the solution of (3), evaluated at time T . This operator represents the noisy implementation of the target circuit $U_L(T)$, in the absence of coherent errors. Furthermore, let $|\tilde{\varrho}\rangle\rangle = \tilde{K}|\rho_0\rangle\rangle$ and $|\varrho^{(\text{id})}\rangle\rangle = U_L(T)|\rho_0\rangle\rangle$ denote the final states associated with \tilde{K} and $U_L(T)$. The incoherent infidelity quantifies the mismatch between $\varrho^{(\text{id})}$ and $\tilde{\varrho}$, and is defined by

$$\varepsilon_{\text{inc}}(\varrho^{(\text{id})}, \tilde{\varrho}) := 1 - F(\varrho^{(\text{id})}, \tilde{\varrho}), \quad (6)$$

$$F(\varrho^{(\text{id})}, \tilde{\varrho}) = \langle\langle \varrho^{(\text{id})}|\tilde{\varrho}\rangle\rangle, \quad (7)$$

where $F(\varrho^{(\text{id})}, \tilde{\varrho})$ is the quantum fidelity [33] between $\varrho^{(\text{id})}$ and $\tilde{\varrho}$ (using the Liouville space formalism, see Eq. (4)). We remark that Eq. (7) is valid for a pure state $\varrho^{(\text{id})}$, which occurs if the initial state ρ_0 is pure. The incoherent infidelity quantifies the effect of noise in the evolution of the initial state $|\rho_0\rangle\rangle$. Thus, if $\varepsilon_{\text{inc}}(\varrho^{(\text{id})}, \tilde{\varrho})$ is too high for a circuit running an algorithm of interest, it indicates an excess of noise that should be handled regardless of the calibration quality of the device. Conversely, error reduction efforts can focus on calibration if the value of $\varepsilon_{\text{inc}}(\varrho^{(\text{id})}, \tilde{\varrho})$ is sufficiently small.

To obtain a more explicit expression for $\varepsilon_{\text{inc}}(\varrho^{(\text{id})}, \tilde{\varrho})$, we solve Eq. (3) in the interaction picture and express the interaction-picture version of \tilde{K} using the Magnus expansion [41]. Details on this derivation are provided in Appendix I. We find that

$$\tilde{K} \approx U_L(T)e^{\Omega_1}, \quad (8)$$

where

$$\Omega_1 = \int_0^T \mathcal{L}^{\text{int}}(t) dt \quad (9)$$

is the first term of the Magnus expansion $\Omega = \sum_{n=1}^{\infty} \Omega_n$, hereafter called “first Magnus term”, and

$$\mathcal{L}^{\text{int}}(t) = U_L^\dagger(t)\mathcal{L}(t)U_L(t) \quad (10)$$

is the representation of $\mathcal{L}(t)$ in the interaction picture. The symbol \cong is used to indicate that we discard higher-order terms in the Magnus expansion. For example, Ω_2 is given by $\Omega_2 = \frac{1}{2} \int_0^T dt' \int_0^{t'} [\mathcal{L}^{\text{int}}(t'), \mathcal{L}^{\text{int}}(t)] dt$. We also note that $U_L(t)$ is the error-free evolution at time t , obtained from Eq. (1).

Since $|\tilde{\varrho}\rangle \cong U_L(T)e^{\Omega_1}|\rho_0\rangle$, according to Eq. (8), we can write

$$F(\varrho^{(\text{id})}, \tilde{\varrho}) \cong \langle \langle \rho_0 | e^{\Omega_1} | \rho_0 \rangle \rangle. \quad (11)$$

Next, we consider the regime of weak noise. This regime is characterized by a rescaling of the dissipator of the form $\mathcal{L}(t) \rightarrow \xi \mathcal{L}(t)$, with a dimensionless parameter ξ such that $\xi \ll 1$. Thus, we can truncate the exponential e^{Ω_1} and keep the linear-order approximation $F(\varrho^{(\text{id})}, \tilde{\varrho}) \cong 1 + \langle \Omega_1 \rangle + O(\xi^2)$, where $\langle \cdot \rangle := \langle \rho_0 | \cdot | \rho_0 \rangle$. This yields

$$\varepsilon_{\text{inc}}(\varrho^{(\text{id})}, \tilde{\varrho}) \cong -\langle \Omega_1 \rangle + O(\xi^2), \quad (12)$$

which is the quantity that we aim to estimate in the following section.

Finally, we stress that there are various fundamental differences between our theory and the general framework of RB. The First difference is that the linear incoherent infidelity (12) constitutes a solid approximation in the regime of weak noise, while RB can handle larger levels of noise. However, under the weak noise condition our method is applicable to target circuits of any size or structure, while RB schemes either benchmark gate sets on average or focus on specific circuits like Clifford gates in the case of Interleaved RB [34]. In addition, it has been noted that Clifford RB faces scalability issues due to errors accumulated in compiled Clifford gates [20]. In Sec. VI, we present scalability conditions that are potentially easier to meet in practical scenarios. Secondly, RB protocols provide error metrics that average out the initial state, while our theory is designed to evaluate the incoherent infidelity given a fixed initial state. Although the simulation of Sec. VB averages the incoherent infidelity over initial states generated by Clifford gates, we do so in order to compare the performance of our method with Interleaved RB, which includes the sampling over initial states as an integral part of its protocol.

IV. EXPERIMENTAL ESTIMATION OF THE INCOHERENT INFIDELITY

In practice, the implementation of the target evolution $U_L(T)$ includes coherent errors. Moreover, simulating the error-free state $\varrho^{(\text{id})}$ becomes infeasible for sufficiently large systems. A direct measurement of the incoherent infidelity is hindered by these obstacles and by state preparation and measurement (SPAM) errors. Here, we propose a method that approximately provides a SPAM-free estimation of the quantity $\langle \Omega_1 \rangle$, which can be used to assess the incoherent infidelity $\varepsilon_{\text{inc}}(\varrho^{(\text{id})}, \tilde{\varrho})$ via Eq. (12).

A. The $K_I K$ composite cycle

Equation (5) represents the actual dynamics that takes place during the execution of the target circuit $U_L(T)$. Denoting this imperfect implementation by K , the building block of our method for extracting the incoherent infidelity is a composite cycle $K_I K$, where K_I is a specific implementation of the inverse unitary $U_L^\dagger(T)$ [42]. In other words, K_I must be such that $K_I = U_L^\dagger(T)$ in the absence of noise and coherent errors. The ideal implementation of K_I and the associated noise are described in Sec. IVB. This results in an extension of the master equation (5) to the total time interval $(0, 2T)$, with K_I being implemented from $t = T$ to $t = 2T$.

An explicit expression for $K_I K$ can be obtained by applying the same strategy that leads to the approximation (8). Namely, by writing (5) in the interaction picture and keeping only the first Magnus term in the corresponding solution. This yields

$$K_I K \cong e^{2\Omega_1 - i\Theta}, \quad (13)$$

where

$$\Theta = \int_0^T U_L^\dagger(t) \delta H(t) U_L(t) dt + \int_T^{2T} U_L^\dagger(2T - t) \delta H(t) U_L(2T - t) dt \quad (14)$$

is the coherent error accumulated during the cycle $K_I K$. More specifically, the first and second integrals in Eq. (14) account for the coherent errors affecting K and K_I , respectively.

To gain some intuition about the use of the composite evolution $K_I K$ for measuring the incoherent infidelity, consider first the linear approximation $e^{2\Omega_1 - i\Theta} \approx I_L + (2\Omega_1 - i\Theta)$. Similarly to what was done with the dissipator, it is now convenient to introduce a rescaling $-i\delta H_L(t) + \mathcal{L}(t) \rightarrow \varsigma [-i\delta H_L(t) + \mathcal{L}(t)]$ that accounts for the strength ς of the total error (coherent and incoherent components). In this way,

$$\begin{aligned} \langle \rho_0 | K_I K | \rho_0 \rangle &\cong 1 + \langle \rho_0 | (2\Omega_1 - i\Theta) | \rho_0 \rangle + O(\varsigma^2) \\ &= 1 + 2\langle \Omega_1 \rangle + O(\varsigma^2), \end{aligned} \quad (15)$$

where the second line follows from the fact that $\langle \rho_0 | \Theta | \rho_0 \rangle = 0$. The proof of this property is given in Appendix II. Equation (15) is equivalent to the expression $\langle \Omega_1 \rangle \cong \frac{1}{2} (\langle \rho_0 | K_I K | \rho_0 \rangle - 1) + O(\varsigma^2)$, which can be used to give a linear estimate of the incoherent infidelity in Eq. (12). While terms of order $O(\xi^2)$ are negligible by assumption, $O(\varsigma^2)$ includes the contribution of the coherent error and thus cannot be directly discarded. To address this issue, in Sec. IVC we consider certain combinations of circuits that correspond to different powers of the cycle $K_I K$. Given a combination $\sum_{k=0}^n a_k^{(n)} (K_I K)^k$, which contains n powers of $K_I K$, it is possible to estimate $\langle \Omega_1 \rangle$ with an error $O(\varsigma^{n+1})$ if the coefficients $a_k^{(n)}$ are properly chosen.

B. Implementation of the inverse evolution K_I

While there are various ways of implementing the inverse of the ideal circuit, we consider the ‘‘pulse inverse’’ K_I generated by the inverse driving [42]

$$H_I(t) = -H(T - t). \quad (16)$$

The use of $H_I(t)$ has a double purpose. In the error-free scenario, it produces the inverse unitary $U_L^\dagger(T)$ when applied during a total time T . Hence, we can guarantee that $K_I = U_L^\dagger(T)$ in this case. On the other hand, the use of $H_I(t)$ is crucial for obtaining the operator $2\Omega_1$ in the approximation (13). Specifically, the first Magnus term associated with the pulse inverse K_I equals the one corresponding to K , and therefore the noise contribution for the cycle $K_I K$ is given by $2\Omega_1$. Such a property allows us to separate the linear quantity $\langle \Omega_1 \rangle$ from higher-order terms in Eq. (15). In contrast, other implementations of $K_I K$ produce a noise contribution $\Omega_1 + \Omega_{I,1}$ to the cycle error, where $\Omega_{I,1}$ stems from K_I and is in general different from Ω_1 . Since the ensuing residual term $\langle \Omega_{I,1} \rangle$ cannot be eliminated by the method presented in Sec. IVC, the pulse inverse K_I is a key element for our estimation of the incoherent infidelity.

Equation (18) relies on Eq. (16) and on the way that the time dependence of $\mathcal{L}(t)$ is affected by the time dependence of $H(t)$. We assume a quasi-stationary time dependence, meaning that the noise does not drift over a certain amount of time t_{\max} . This condition implies that, for $t \leq t_{\max}$, any cycle involving $H(t)$ is subjected to the same dissipator $\mathcal{L}(t)$. That is,

$$\mathcal{L}(t + 2mT) = \mathcal{L}(t), \quad (17)$$

for some positive integer such that $t + 2mT \leq t_{\max}$. Here, the time period $2T$ expresses the fact that in circuit sequences involving the cycle $K_I K$ the driving $H(t)$ would be repeated after $2T$. As explained in Sec. IVC, these sequences constitute the circuits to be executed for our evaluation of the incoherent infidelity. The total time for the implementation of such circuits must also be smaller than t_{\max} , to guarantee the fulfillment of the condition (17).

The time dependence of $\mathcal{L}(t)$ can be arbitrary so long as it satisfies Eq. (17). In particular, our approach admits noise mechanisms that can affect different gates in varying ways. An example of this is leakage noise in systems where the qubit is encoded in two levels of a larger Hilbert space, as in superconducting qubits. This leakage noise will depend in general on the non-adiabatic character of the driving $H(t)$.

Keeping in mind the irreversible character of noise, we consider that the instantaneous effect of $\mathcal{L}(t)$ remains unchanged when the sign of the Hamiltonian is reversed. Thus, $H(t)$ and $-H(t)$ give rise to the same dissipator $\mathcal{L}(t)$. In combination with Eq. (16), this argument leads to the relationship

$$\mathcal{L}_I(t) = \mathcal{L}(T - t), \quad (18)$$

where $\mathcal{L}_I(t)$ is the dissipator that acts alongside the driving $H_I(t)$. The condition of quasi-stationary noise is also applicable in this case, meaning that $\mathcal{L}_I(t + 2mT) = \mathcal{L}_I(t)$ if $t + 2mT \leq t_{\max}$.

To have a clearer picture of Eq. (18), consider a discrete set of (possibly time dependent) dissipators $\{\mathcal{L}_i\}_{i=0}^N$ that act on gates executed at different times $\{t_i\}_{i=0}^N$. If these gates are generated by $H(t)$, the inverse pulse $H_I(t)$ not only produces the corresponding inverse gates, but also reverses their time order. Therefore, under $H_I(t)$ the noise mechanism that acts at time t_j is not \mathcal{L}_j but \mathcal{L}_{N-j} . Equation (18) captures this reverse ordering in a time-continuous fashion.

We note that Eqs. (16) and (18) describe the action of $H_I(t)$ and $\mathcal{L}_I(t)$ in a time interval $(0, T)$. To construct the cycle $K_I K$, the driving $H_I(t)$ must be implemented between $t = T$ and $t = 2T$. Therefore, when extending the master equation (5) to cover the total interval $(0, 2T)$, we must perform the replacements $H_L(t) \rightarrow H_I(t-T) \otimes I - I \otimes H_I(t-T)^T$ and $\mathcal{L}(t) \rightarrow \mathcal{L}_I(t-T)$ for $T \leq t \leq 2T$. On the other hand, $\delta H_L(t)$ can feature an arbitrary time dependence, without requiring any particular relation between the coherent errors affecting the evolutions K and K_I .

C. Evaluating the incoherent infidelity using multiple $K_I K$ cycles

In this section, we present our procedure for assessing the incoherent infidelity. We start by defining the quantities

$$\begin{aligned} R_k &:= \langle\langle \rho_k | \rho_0 \rangle\rangle \\ &= \langle\langle \rho_0 | (K_I K)^k | \rho_0 \rangle\rangle, \end{aligned} \quad (19)$$

where $|\rho_k\rangle\rangle = (K_I K)^k |\rho_0\rangle\rangle$, and

$$\begin{aligned} \sigma_n &:= \sum_{k=0}^n a_k^{(n)} \langle\langle \rho_0 | (K_I K)^k | \rho_0 \rangle\rangle \\ &= \sum_{k=0}^n a_k^{(n)} R_k \\ &\cong \sum_{k=0}^n a_k^{(n)} \langle\langle \rho_0 | e^{k\chi} | \rho_0 \rangle\rangle. \end{aligned} \quad (20)$$

The third line follows from the approximation (13), and we also define $\chi := 2\Omega_1 - i\Theta$. In the case of a pure initial state ρ_0 , R_k is the survival probability measured after k cycles $K_I K$. Namely, the probability that the system is found in the initial state when the circuit $(K_I K)^k$ is executed.

Assuming that the operator χ is diagonalizable, an eigenvalue of $(K_I K)^k$ has the form e^{kx} , where x is an eigenvalue of χ . Notice that x is a complex number in general. Furthermore, $\sum_{k=0}^n a_k^{(n)} (K_I K)^k$ has a corresponding eigenvalue given by $\lambda(x) := \sum_{k=0}^n a_k^{(n)} e^{kx}$. For sufficiently weak noise and coherent errors the cycle $K_I K$ is close to the identity operator I_L , and therefore the norm of x satisfies $|x| \ll 1$. Thus, we can approximate any eigenvalue $\lambda(x)$ by a truncated Taylor series around $x = 0$.

For reasons that will shortly be clarified, our goal is to approximate x through $\lambda(x)$. The quality of this approximation will depend on the maximum number of cycles n in the circuit combination $\sum_{k=0}^n a_k^{(n)} (K_I K)^k$. To obtain this approximation, we impose the conditions

$$\left(\frac{d^j}{dx^j} \lambda \right)_{x=0} = 0, \quad j = 0, 2, 3, \dots, n, \quad (21)$$

$$\left(\frac{d}{dx} \lambda \right)_{x=0} = 1, \quad (22)$$

which lead to the truncated Taylor expansion

$$\lambda(x) = x + \frac{(-1)^{n+1}}{n+1} x^{n+1} + O(x^{n+2}). \quad (23)$$

By rescaling each eigenvalue x as $x \rightarrow \varsigma x$, we can combine Eqs. (20) and (23) to obtain

$$\begin{aligned} \sigma_n &\cong \langle\chi\rangle + \frac{(-1)^{n+1}}{n+1} \langle\chi^{n+1}\rangle + O(\varsigma^{n+2}) \\ &= 2\langle\Omega_1\rangle + \frac{(-1)^{n+1}}{n+1} \langle\chi^{n+1}\rangle + O(\varsigma^{n+2}). \end{aligned} \quad (24)$$

In the second line of Eq. (24) we write $\langle \chi \rangle = 2 \langle \Omega_1 \rangle$, using the already mentioned property $\langle \langle \rho_0 | \Theta | \rho_0 \rangle \rangle = 0$. By combining Eq. (24) with Eq. (12), we arrive to our main result:

$$\varepsilon_{\text{inc}}(\varrho^{(\text{id})}, \tilde{\varrho}) \cong -\frac{\sigma_n}{2} + O(\zeta^{n+1}) + O(\xi^2). \quad (25)$$

This implies that the incoherent infidelity can be estimated with higher accuracy by increasing n . The measurement of σ_n involves implementing the circuits $(K_I K)^k$, for $0 \leq k \leq n$, measuring the corresponding quantities R_k , and computing the weighted sum $\sum_{k=0}^n a_k^{(n)} R_k$. In practice, the convergence of σ_n within a given experimental precision determines the maximum value of n . This means that, once $|\sigma_{n+1} - \sigma_n|$ is smaller than the target experimental uncertainty, it is not practical to keep increasing n . For clarity, we also mention that the variance in the estimation of σ_n can be reduced by performing a sufficient number of shots (executions) of the circuits $(K_I K)^k$.

D. Explicit form of the coefficients $a_k^{(n)}$

Let us now discuss the explicit form of the coefficients $a_k^{(n)}$ that are obtained from Eqs. (21) and (22). These equations are equivalent to the linear system

$$\sum_{k=0}^n k^j a_k^{(n)} = 0, \quad j = 0, 2, 3, \dots, n, \quad (26)$$

$$\sum_{k=0}^n k a_k^{(n)} = 1. \quad (27)$$

Such a system can be conveniently written as

$$(a_0^{(n)}, a_1^{(n)}, a_2^{(n)}, \dots, a_n^{(n)}) V_n = (0, 1, 0, \dots, 0), \quad (28)$$

where

$$V_n = \begin{pmatrix} 1 & 0 & 0 & \dots & 0 \\ 1 & 1^1 & 1^2 & \dots & 1^n \\ 1 & 2^1 & 2^2 & \dots & 2^n \\ \dots & \dots & \dots & \dots & \dots \\ 1 & n & n^2 & \dots & n^n \end{pmatrix}. \quad (29)$$

is an $(n+1) \times (n+1)$ Vandermonde matrix. Accordingly, the solution to the coefficients $a_k^{(n)}$ corresponds to the second row of the inverse of V_n . If the elements $(V_n^{-1})_{j,k}$ of this inverse are identified with indexes $1 \leq j, k \leq n+1$, we have that

$$a_k^{(n)} = (V_n^{-1})_{2,k+1}. \quad (30)$$

In particular, for $1 \leq n \leq 4$ we obtain:

$$\sigma_1 = -R_0 + R_1, \quad (31)$$

$$\sigma_2 = -\frac{3}{2}R_0 + 2R_1 - \frac{1}{2}R_2, \quad (32)$$

$$\sigma_3 = -\frac{11}{6}R_0 + 3R_1 - \frac{3}{2}R_2 + \frac{1}{3}R_3, \quad (33)$$

$$\sigma_4 = -\frac{25}{12}R_0 + 4R_1 - 3R_2 + \frac{4}{3}R_3 - \frac{1}{4}R_4. \quad (34)$$

As we shall see in Sec. V, while $\sigma_1 = R_1 - R_0$ turns out to be specially sensitive to coherent errors, $\sigma_{n \geq 2}$ provides an accurate estimation of the incoherent infidelity.

E. Robustness to SPAM errors

SPAM errors are errors that occur in the preparation of the initial state and in the measurement of the final state. A desirable characteristic of any benchmarking tool is that it can separate the SPAM contribution from the total error, in order to provide a reliable quantification of the errors associated with the evolution, i.e. the circuit. We show that the measurement of σ_n is robust to SPAM errors that are comparable to the errors encapsulated by χ . In this way, the estimation of the incoherent infidelity is also robust to this kind of SPAM errors.

Let U_p be the ideal (error-free) evolution that is used to prepare the pure state $|\rho_0\rangle\rangle$. If the fiducial state is denoted by $|0\rangle\rangle$, we have that $|\rho_0\rangle\rangle = U_p|0\rangle\rangle$. Note that while here we are not using the subindex L to indicate that U_p is a unitary in Liouville space, this is understood from the context. Similarly, an ideal measurement of the state ρ_0 is described by the row vector $\langle\langle\rho_0| = \langle\langle 0|U_p^\dagger$. In the error-free scenario, $R_k = \langle\langle 0|U_p^\dagger(K_I K)^k U_p|0\rangle\rangle$ would be measured by executing the circuit $U_p^\dagger(K_I K)^k U_p$ and measuring the fiducial state $|0\rangle\rangle$. However, instead of the perfect unitaries U_p and U_p^\dagger what is implemented in practice are error-prone circuits K_p and K_m , where the subscripts p and m stand for preparation and measurement, respectively. These evolutions can be written as (see Appendix III)

$$K_p = U_p e^{\Omega_p}, \quad (35)$$

$$K_m = e^{\bar{\Omega}_m} U_p^\dagger, \quad (36)$$

$$\bar{\Omega}_m = U_p^\dagger \Omega_m U_p \quad (37)$$

where Ω_p (Ω_m) is the Magnus expansion that characterizes preparation (measurement) errors. We remark that Eqs. (35) and (36) represent the exact solutions for K_p and K_m , since they include the full Magnus expansions and not only the first Magnus terms. Importantly, Ω_p and $\bar{\Omega}_m$ fully incorporate noise and coherent errors in the preparation and measurement stages, and in general $\bar{\Omega}_m$ and Ω_p are unrelated to each other.

In this way, under SPAM errors the quantity that is measured when trying to estimate σ_n is

$$\begin{aligned} \sigma'_n &= \sum_{k=0}^n a_k^{(n)} R'_k \\ &= \sum_{k=0}^n a_k^{(n)} \langle\langle 0|K_m(K_I K)^k K_p|0\rangle\rangle. \end{aligned} \quad (38)$$

In Appendix III, we show that

$$|\sigma'_n - \sigma_n| = O(\|\Omega_m\| \|\chi\| + \|\Omega_p\| \|\chi\|), \quad (39)$$

where $\|\cdot\|$ denotes the spectral norm. This follows from the fact that any contribution to $|\sigma'_n - \sigma_n|$ involves products of the form $\|\Omega_m\|^k \|\Omega_p\|^l \|\chi\|^m$, with $k+l \geq 1$ and $m \geq 1$. Since we assume weak errors $\|\chi\|, \|\Omega_p\|, \|\Omega_m\| \ll 1$, these contributions are negligible, and the dominant terms in the difference between σ'_n and the SPAM-free quantity σ_n are the quadratic corrections $\|\Omega_m\| \|\chi\|$ and $\|\Omega_p\| \|\chi\|$. Crucially, while each R'_k has a correction term which is $O(\|\Omega_p\|, \|\Omega_m\|)$, these leading order corrections cancel out when calculating σ'_n and the SPAM corrections enter only in second order. Finally, we remark that Eq. (39) holds whenever σ'_n contains all the terms affected by SPAM errors, including $R'_0 = \langle\langle 0|K_m K_p|0\rangle\rangle$. Therefore, R'_0 must also be measured and cannot simply be replaced by its ideal value $R_0 = 1$. We have avoided writing 1 instead of R_0 in Eqs. (31)-(34), to further emphasize this fact.

In the case of readout errors, it is also possible to complement our method with techniques that mitigate their impact and help to achieve the regime of SPAM robustness characterized in Sec. IVE. In particular, Appendix IV discusses how to mitigate local readout errors in a simple and scalable manner. Such strategy would allow us to efficiently estimate the incoherent infidelity in large systems, where local readout errors may be substantial, so long as correlated readout errors remain sufficiently small.

V. ILLUSTRATIVE EXAMPLES

We illustrate now our technique for measuring the incoherent infidelity using two numerical examples. In Fig. 1, we consider the incoherent infidelity associated with noise in the circuit that generates a five-qubit GHZ (Greenberger–Horne–Zeilinger) state. The second example, illustrated in Fig. 2, refers to the evaluation of the *average* incoherent infidelity of a CNOT gate. While the example of Fig. 1 does not include SPAM errors, we do so in the second example.

The analysis of the GHZ state is mainly aimed to show the resilience of our method to coherent errors, depicted in Fig. 1 by the convergence of our estimation to the actual value of $\varepsilon_{\text{inc}}(\varrho^{(\text{id})}, \tilde{\varrho})$. The second example involves the estimation of the gate incoherent infidelity, obtained by averaging over a set of initial states. We consider specifically input states generated by error-prone Clifford gates, as well as SPAM errors in the fiducial state and readout errors. This example demonstrates the robustness of our method to the associated SPAM errors. In addition, it serves to illustrate how our technique can also be used to evaluate the average incoherent error of a target circuit.

For simplicity, the unitary evolutions in this section will be written using the traditional notation. That is, as unitary operators that act on quantum states in Hilbert space.

A. Estimating the incoherent infidelity for the preparation of a five-qubit GHZ state

The five-qubit GHZ state can be prepared by using a circuit composed of a Hadamard gate and four CNOT gates. We remark that in this example the initial state is the fiducial state $|0\rangle$, and the circuit that prepares the GHZ state represents the target evolution that we want to assess. To simulate the execution of this circuit in a real physical system, we consider the cross-resonance interaction employed for the CNOT gate in some superconducting qubits [43]. Letting $\{X, Y, Z\}$ denote the Pauli matrices, the cross resonance interaction between the qubits j and k is given by $Z_j \otimes X_k$, where Z_j is the Z Pauli matrix applied on qubit j , and X_k is the X Pauli matrix applied on qubit k . By combining it with local rotations, this interaction leads to the following CNOT unitary

$$U_{\text{CNOT}}^{(j,k)} = e^{i\frac{\pi}{4}X_k} e^{-i\frac{\pi}{4}Z_j \otimes X_k} e^{i\frac{\pi}{4}Z_j}, \quad (40)$$

where j is the control qubit and k is the target qubit.

The imperfect preparation of the GHZ state is simulated by including errors that act during the cross resonance pulse. On the other hand, we assume error-free implementations for the single-qubit rotations $e^{i\frac{\pi}{4}X_k}$ and $e^{i\frac{\pi}{4}Z_j}$, and for the Hadamard gate. Noise is characterized by dephasing and amplitude damping channels that act identically on the five qubits used to prepare the GHZ state, as described in Appendix V. For the coherent errors, we consider the cross talk term [27]

$$\delta H^{(j,k)} = \eta Z_j \otimes Z_k, \quad (41)$$

which affects the ideal cross resonance interaction $Z_j \otimes X_k$. The parameter η characterizes the strength of this error contribution. Note that since the interaction (41) is not controllable, η does not change its sign when implementing the pulse inverse.

We simulate the estimation of the incoherent infidelity by computing σ_n in Eq. (20). In this case, the circuit K corresponds to the error-prone circuit used to prepare the GHZ state, and K_I is the associated inverse. The incoherent infidelity $\varepsilon_{\text{inc}}(\varrho^{(\text{id})}, \tilde{\varrho})$ is estimated by $-\sigma_n/2$, according to Eq. (25). For (incoherent) infidelities around 0.05, our simulations yield estimations of ~ 0.04 using $-\sigma_n/2$, for $n \sim 5$. However, for the sake of demonstration, we consider smaller infidelities in the example of Fig. 1, such that $-\sigma_n/2$ virtually converges to ε_{inc} .

The initial state ρ_0 is the five-qubit ground state (where all the qubits are in the “0” state), and, for simplicity of demonstration, we do not consider SPAM errors. In this way, we can focus on the robustness of our method to coherent errors, which is the main purpose of this simulation. Moderate SPAM errors can be added without affecting the outcome of the simulation. This is illustrated in the example presented in Sec. VB.

The simulation parameters are chosen as follows. To obtain the ideal CNOTs in the error-free case, we set the evolution time for the cross resonance interaction to $T = \pi/4$. The coherent error parameter η is such that $\eta T = 0.0312$, in Fig. 1(a), and $\eta T = 0.02$ for Fig. 1(b). In Appendix V, we also introduce a parameter ξ that characterizes the strength of the noise ($\xi = 0$ corresponds to zero noise) and set it to $\xi T = 0.0035$ and $\xi T = 0.000351$ for Figs. 1(a) and 1(b), respectively. These values of η and ξ are low enough to maintain consistency with the approximations intrinsic to our method.

The results presented in Fig. 1 show convergence of $-\sigma_n/2$ to the actual value of $\varepsilon_{\text{inc}}(\varrho^{(\text{id})}, \tilde{\varrho})$ (dashed red lines), at approximately $n = 5 K_I K$ cycles. Thus, they provide numerical evidence of the accuracy achieved by our method, in the regime of weak noise. In Sec. VI, we precisely define this noise regime and characterize the corresponding accuracy. The big difference between $-\sigma_1/2$ and $\varepsilon_{\text{inc}}(\varrho^{(\text{id})}, \tilde{\varrho})$ indicates that the linear order approximation (15) is not sufficient to suppress the effect of coherent errors in the calculation of $\varepsilon_{\text{inc}}(\varrho^{(\text{id})}, \tilde{\varrho})$. As n increases, this effect is systematically mitigated, and we can obtain an accurate estimation of the incoherent infidelity. We also note that the relative error for the estimation using σ_1 is substantially larger in Fig. 1(b). This can be explained by the fact that the coherent error strength is not much smaller than the corresponding to Fig. 1(a), while the noise strength is

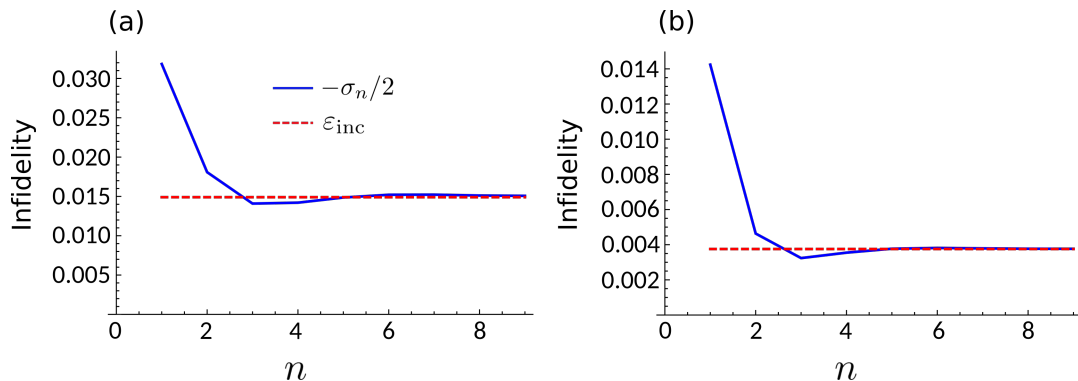


Figure 1. Incoherent infidelity for the implementation of a five-qubit GHZ state. The dashed red lines depict the exact value and the solid blue lines correspond to the estimation using σ_n (cf. Eq. (25)), as a function of the number of cycles $K_I K$ (denoted by n). (a) Simulation parameters are $\eta T = 0.0312$ and $\xi T = 0.0035$, where T is the evolution time of the cross resonance interaction, η characterizes the strength of coherent errors, and ξ characterizes the noise strength. (b) In this case, we set $\eta T = 0.02$ and $\xi T = 0.000351$.

reduced by one order of magnitude. Therefore, the first-order ($n = 1$) estimation of the incoherent infidelity is more affected by coherent errors in Fig. 1(b). However, in both cases increasing n fixes this problem and leads to fast convergence to $\varepsilon_{\text{inc}}(\varrho^{(\text{id})}, \tilde{\varrho})$.

B. Estimating the average incoherent infidelity for a CNOT gate affected by SPAM errors

In this example, the target circuit is a CNOT gate which acts on qubits labeled by $j = 1$ and $k = 2$. Rather than estimating the incoherent infidelity associated with a single initial state ρ_0 , we consider the average over many randomly chosen (two-qubit) Clifford gates employed for preparation and measurement. Specifically, in Fig. 2 we present results for $M = 300$ different initial states obtained from these gates. In methods like Interleaved RB, this averaging is useful to tailor the noise into a global depolarizing channel, from which it is possible to extract the error per gate. However, such a noise tailoring can be hampered by coherent errors in the Clifford gates used for preparation and measurement. While it has been shown that this can cause an incorrect estimation of the error rate [44], in the following example we illustrate that this is not the case with the present method.

The average incoherent infidelity is defined as

$$\bar{\varepsilon}_{\text{inc}} := \frac{1}{M} \sum_{m=1}^M \varepsilon_{\text{inc}}(\varrho_m^{(\text{id})}, \tilde{\varrho}_m), \quad (42)$$

where $\varrho_m^{(\text{id})}$ and $\tilde{\varrho}_m$ are states corresponding to the m th preparation. More precisely, $\varrho_m^{(\text{id})}$ is the error-free final state and $\tilde{\varrho}_m$ is the state obtained when the target evolution only contains noise and no coherent errors. We also stress that, for capturing the errors associated with the gate, SPAM errors are absent in the computation of the exact infidelity (42), as per the definition given in Eq. (6). However, they are included in the simulated estimation of the average incoherent infidelity.

To simulate the estimation of $\bar{\varepsilon}_{\text{inc}}$, we include coherent errors and noise that afflict $U_{\text{CNOT}}^{(1,2)}$ as well as the Clifford gates used for preparation and measurement. SPAM errors contain also a contribution that is relevant for quantum computing architectures such as the one used by IBM. Concretely, we refer to readout errors [45, 46] and potential errors in the preparation of the fiducial state $|0\rangle$ [47]. Our modeling of these errors is based on Reference [47], and is described in Appendix V. In combination with the errors affecting the Clifford gates for preparation and measurement, they constitute the SPAM errors for the simulation presented below.

All the CNOT gates are subjected to the coherent error (41), and we shall use the angle $\phi = \eta T$ to characterize the associated error strength. In addition, following Reference [44], we introduce another coherent error that affects single-qubit gates. Specifically, let $R_W(\alpha) = e^{-i\frac{\alpha}{2}W}$ denote a single-qubit rotation by an angle α , around some “axis” $W \in \{X, Y, Z\}$ of the Bloch sphere. We consider the following modification of the error-free rotations $R_W(\pm\pi/2)$, for $W = X, Y$ [44]:

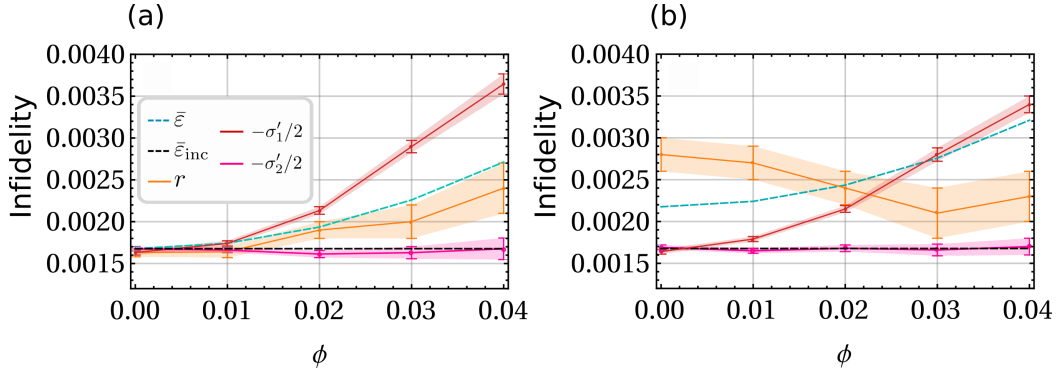


Figure 2. Average incoherent infidelity and average infidelity for the implementation of a CNOT gate. These averages are taken over $M = 300$ two-qubit Clifford gates, employed for the preparation of the initial state. In these plots, $\bar{\varepsilon}$ is the exact infidelity (45), r is the estimate of $\bar{\varepsilon}$ using Interleaved RB, and $\bar{\varepsilon}_{\text{inc}}$ is the exact incoherent infidelity (42). Moreover, $-\sigma'_1/2$ and $-\sigma'_2/2$ are estimates of $\bar{\varepsilon}_{\text{inc}}$ that involve SPAM errors. The error bars correspond to one standard deviation when only one measurement is performed per each Clifford gate. In (a) and (b), the single-qubit coherent error is set to $\theta = 0$ and $\theta = 0.05$, respectively.

$$R_W(\pi/2) \rightarrow e^{-i\theta Z} R_W(\pi/2), \quad (43)$$

$$R_W(-\pi/2) \rightarrow R_W(-\pi/2) e^{i\theta Z}. \quad (44)$$

Importantly, any single-qubit Clifford gate can be compiled using sequences of the ideal gates $R_X(\pm\pi/2)$ and $R_Y(\pm\pi/2)$. Furthermore, it was shown in [44] that RB is sensitive to the coherent error described by Eqs. (43) and (44). This error is added to any single-qubit Clifford gate in our simulation, including the R_X gate in the target CNOT. Regarding noise, only the cross resonance pulse (cf. Eq. (40)) in the CNOT gates is affected by local dephasing and amplitude damping. A complete description of all these error sources can be found in Appendix V.

In Fig. 2, we plot $-\sigma'_1/2$ (solid red curves) and $-\sigma'_2/2$ (solid purple curves) as a function of the angle ϕ , for values $\phi \in \{0, 0.01, 0.02, 0.03, 0.04, 0.05\}$. Moreover, the noise strength is chosen such that $\xi T = 0.001$. In addition to the incoherent infidelity, we also apply Interleaved RB [34] to estimate the average infidelity of the target CNOT gate. Details about this estimation are given in Appendix VI. As opposed to our method, the infidelity obtained via Interleaved RB aims to encompass all the error sources and not only the contribution from noise. This means that, instead of $\varepsilon_{\text{inc}}(\varrho_m^{(\text{id})}, \tilde{\varrho}_m)$, the infidelity corresponding to the m -th preparation is $\varepsilon(\varrho_m^{(\text{id})}, \varrho_m) = 1 - F(\varrho_m^{(\text{id})}, \varrho_m)$, where ϱ_m is the actual final state that results from the application of K . Thus, the estimation of

$$\bar{\varepsilon} := \frac{1}{M} \sum_{m=1}^M \varepsilon(\varrho_m^{(\text{id})}, \varrho_m) \quad (45)$$

is the relevant reference for evaluating the performance of Interleaved RB.

The angle θ is set to $\theta = 0$ and $\theta = 0.05$ in Figs. 2(a) and 2(b), respectively. In both cases, we observe that the estimation of $\bar{\varepsilon}$ via Interleaved RB (solid orange curves) significantly deviates from the exact value (dashed cyan curves). This is specially noticeable in Fig. 2(b), where the deviation is clear even for $\phi = 0$. Such a mismatch is an indication that either coherent errors are not properly addressed in the Interleaved RB method, or that the error rate that it measures cannot always be associated with the infidelity. On the other hand, Fig. 2 shows that $-\sigma'_2/2$ (solid magenta curves) approaches well the incoherent infidelity $\bar{\varepsilon}_{\text{inc}}$ (dashed black curves), irrespective of the type of coherent errors included. We also emphasize that SPAM errors are fully taken into account in the simulation of $-\sigma'_1/2$ (solid red curves) and $-\sigma'_2/2$. Thus, the proximity of $-\sigma'_2/2$ and $\bar{\varepsilon}_{\text{inc}}$ illustrates the resilience of our estimation to SPAM errors. Finally, we remark that, similarly to Fig. 1, the linear approximation $-\sigma'_1/2$ fails to provide a good estimate of the incoherent infidelity. However, with only two $K_I K$ cycles we obtain the accurate estimation observed in Fig. 2, which is specially evident by the overlap between the magenta curve and the dashed black curve in Fig. 2(b).

To conclude this section, we point out that for each initial state the measurement of σ'_n yields an estimate of the incoherent infidelity associated with that specific input. This contrasts with Interleaved RB and other benchmarking tools for target circuits, where measurement data can only provide estimates of the circuit infidelity. In other words,

although Eq. (45) is defined in terms of the single-realization quantities $\varepsilon(\varrho_m^{(\text{id})}, \varrho_m)$, it is not possible to assess these infidelities via Interleaved RB. Only the average $\bar{\varepsilon}$ can be estimated. Our method is not restricted by this limitation and could also be useful to learn about the noise fluctuations associated with different initial conditions. In particular, by comparing different infidelities $\varepsilon_{\text{inc}}(\varrho_m^{(\text{id})}, \tilde{\varrho}_m)$ between each other and with the average infidelity $\bar{\varepsilon}_{\text{inc}}$, one could study how input states influence circuit performance and use this information for the design of effective error suppression strategies.

VI. CONDITIONS FOR THE SCALABILITY OF THE INCOHERENT INFIDELITY ESTIMATION

In this section, we provide error bounds for the approximations (12) and (13). We argue that if the relevant error parameters are small (as required for the validity of our approximations), our method is scalable within the accuracy established by these bounds. Specifically, we require that the accumulated noise and coherent errors should remain sufficiently low as the circuit size increases. This is a valid prerequisite for performing useful computations in the NISQ era, where a systematic application of error correction is not yet available [48]. To characterize this condition in our formalism, we set limits to the quantities $\int_0^T dt \|\mathcal{L}_{\text{ext}}(t)\|$ and $\int_0^{2T} dt \|\mathcal{L}_{\text{ext}}(t) - i\delta H_L(t)\|$, introduced in Eqs. (49) and (50).

For clarity, we are going to denote by $\Omega(T)$ and $\Omega(2T)$ the Magnus expansions associated with K and $K_I K$, respectively. In addition, we write the dissipator that characterizes the noise in the extended time interval $(0, 2T)$ as $\mathcal{L}_{\text{ext}}(t)$. Therefore, the equation that governs the cycle $K_I K$ reads

$$d_t |\rho\rangle\rangle = (-iH_{L,\text{ext}}(t) - i\delta H_L(t) + \mathcal{L}_{\text{ext}}(t)) |\rho\rangle\rangle, \quad (46)$$

where

$$H_{L,\text{ext}}(t) = \begin{cases} H_L(t), & \text{for } t \in (0, T), \\ H_I(t-T) \otimes I - I \otimes H_I^T(t-T), & \text{for } t \in (T, 2T), \end{cases} \quad (47)$$

and

$$\mathcal{L}_{\text{ext}}(t) = \begin{cases} \mathcal{L}(t), & \text{for } t \in (0, T), \\ \mathcal{L}_I(t-T), & \text{for } t \in (T, 2T). \end{cases} \quad (48)$$

The error bounds presented in Eqs. (49) and (50) are derived in Appendix VII. In the case of Eq. (50), we have a bound that quantifies how close the approximation e^x is to the exact evolution $K_I K = e^{\Omega(2T)}$. The accuracy of this approximation is directly related to the accuracy for estimating the incoherent infidelity using $K_I K$ cycles. More precisely, note that the right hand side of Eq. (24) is based on Eq. (13), but the definition of σ_n (first line of Eq. (20)) and its estimation rely on circuits that contain the actual cycle $K_I K$. Therefore, the closer $K_I K$ to e^x , the better the estimation of $\varepsilon_{\text{inc}}(\varrho^{(\text{id})}, \tilde{\varrho})$ by using σ_n . We also emphasize that since many inequalities are involved in the derivation of (49) and (50), it is probable that these bounds substantially overestimate the actual errors. As a result, the regime of validity of our method is expected to be larger than predicted by these bounds.

The error in approximating the incoherent infidelity by (12) is given by $|\varepsilon_{\text{inc}}(\varrho^{(\text{id})}, \tilde{\varrho}) + \langle \Omega_1 \rangle|$. Importantly, this error quantifies the difference between $-\langle \Omega_1 \rangle$ and the *exact* incoherent infidelity $\varepsilon_{\text{inc}}(\varrho^{(\text{id})}, \tilde{\varrho}) = 1 - \langle \langle \rho_0 | e^{\Omega(T)} | \rho_0 \rangle \rangle$, expressed in terms of the *full* Magnus expansion $\Omega(T)$. In Appendix VII, we derive the bound

$$\left| \varepsilon_{\text{inc}}(\varrho^{(\text{id})}, \tilde{\varrho}) + \langle \Omega_1 \rangle \right| \leq e^{\int_0^T dt \|\mathcal{L}_{\text{ext}}(t)\|} - \int_0^T dt \|\mathcal{L}_{\text{ext}}(t)\| - 1. \quad (49)$$

The quantity $\int_0^T dt \|\mathcal{L}_{\text{ext}}(t)\| = \int_0^T dt \|\mathcal{L}(t)\|$ in this bound can be interpreted as the total noise affecting the evolution K , and is such that $\int_0^T dt \|\mathcal{L}(t)\| = O(\xi) \ll 1$ in the weak noise regime. In particular, for $\int_0^T dt \|\mathcal{L}(t)\| \leq 0.05$ we have that $|\varepsilon_{\text{inc}}(\varrho^{(\text{id})}, \tilde{\varrho}) + \langle \Omega_1 \rangle| \leq 0.001$, according to Eq. (49).

Crucially, an expansion of the right hand side of Eq. (49) shows that this bound is $O(\xi^2)$. On the other hand, in the regime of weak noise the incoherent infidelity is linear in $\mathcal{L}(t)$, as per Eqs. (9)-(12). This indicates that, in this regime, the error in the estimation of $\varepsilon_{\text{inc}}(\varrho^{(\text{id})}, \tilde{\varrho})$ is substantially smaller than the estimated incoherent infidelity.

In the case of Eq. (50), we quantify the error using the spectral norm of the difference between $K_I K$ and the approximation $e^{2\Omega_1 - i\Theta}$ in Eq. (13). Since the error-free evolution corresponding to $K_I K$ is the identity operator, we have that $K_I K = e^{\Omega(2T)}$. It is also worth noting that $\chi = 2\Omega_1 - i\Theta$ is the first Magnus term of the expansion $\Omega(2T)$, as explained in Appendix I. The relevant error bound is given by

$$\left\| e^{\Omega(2T)} - e^\chi \right\| \leq 2 \left(e^{\int_0^{2T} dt \|\mathcal{L}_{\text{ext}}(t) - i\delta H_L(t)\|} - \int_0^{2T} dt \|\mathcal{L}_{\text{ext}}(t) - i\delta H_L(t)\| - 1 \right). \quad (50)$$

Here, we identify $\int_0^{2T} dt \|\mathcal{L}_{\text{ext}}(t) - i\delta H_L(t)\|$ with the total evolution error for $K_I K$, including the coherent contribution from $\delta H_L(t)$. Keeping in mind that $K_I K$ takes twice the time invested by K , we assume that $\int_0^{2T} dt \|\mathcal{L}_{\text{ext}}(t) - i\delta H_L(t)\| \gtrsim 2 \int_0^T dt \|\mathcal{L}_{\text{ext}}(t)\|$. Thus, as maximum reference value for $\int_0^{2T} dt \|\mathcal{L}_{\text{ext}}(t) - i\delta H_L(t)\|$ we consider $\int_0^{2T} dt \|\mathcal{L}_{\text{ext}}(t) - i\delta H_L(t)\| = 0.1$, keeping in mind that before we assumed $\int_0^T dt \|\mathcal{L}_{\text{ext}}(t)\| \leq 0.05$. By inserting this error limit into Eq. (50), we find that $\|e^{\Omega(2T)} - e^\chi\| \leq 0.01$. In analogy with Eq. (49), we also remark that the dominant contribution to the bound (50) is the quadratic term $2 \left(\int_0^{2T} dt \|\mathcal{L}_{\text{ext}}(t) - i\delta H_L(t)\| \right)^2$.

VII. CONCLUSIONS

In this paper, we have developed a method for estimating the impact of noise on the fidelity of a target quantum evolution. To this end, we introduced the ‘‘incoherent infidelity’’, as a measure of the infidelity that excludes the contribution from coherent errors affecting the tested circuit. Our technique is designed to evaluate the performance of a given target evolution, with respect to a given initial state, or as an average over a set of initial states. These features are specially relevant if the goal is to benchmark a certain quantum algorithm or quantum computation, rather than the overall performance of a quantum device. In particular, our estimation of the incoherent infidelity can be applied to quantum algorithms whose success depends on validating the quality of some specific output, or outputs.

We presented numerical simulations that highlight different aspects of our estimation of the incoherent infidelity. By simulating errors in the preparation of a five-qubit GHZ state, we illustrated its robustness to coherent errors. Another example involved the estimation of the incoherent infidelity for a CNOT gate. In this case, we computed the average infidelity over a set of random initial states prepared by Clifford gates. We have shown analytically that the incoherent infidelity estimation is also resilient to SPAM errors of moderate magnitude, and corroborated this property in our simulation. We modeled SPAM errors by considering an imperfect fiducial state and readout errors, as well as noise and coherent errors in the Clifford gates employed for preparation and measurement.

Our method does not require the classical simulation of the error-free state generated by the target circuit. Furthermore, there is no restriction on the target evolution and the gates that compose it. It also admits a simple experimental implementation, and the number of measurements to achieve a certain accuracy is independent of the size of the system. Therefore, it provides a scalable tool to assess the incoherent infidelity in the weak noise regime, where our theory is valid.

An open problem is the extension of this technique to cover larger error rates. However, it is worth keeping in mind that, in the absence of quantum error correction, the errors accumulated in quantum computers must be low enough to allow useful computations. Under this restriction, we believe that our technique can be used to benchmark quantum algorithms with the potential of a practical quantum advantage. We also anticipate that it can be combined with other benchmarking tools for obtaining additional information about different classes of errors. For example, it might be possible to estimate the strength of coherent errors if the incoherent infidelity is complemented with estimates of the total infidelity (as proposed e.g. in Reference [36]).

VIII. ACKNOWLEDGMENTS

Raam Uzdin is grateful for support from the Israel Science Foundation (Grant No. 2556/20).

IX. DATA AVAILABILITY STATEMENT

All the information relevant for our simulations is included in the plots within the main text and the appendices.

* raam@mail.huji.ac.il

- [1] F. Arute, K. Arya, R. Babbush, D. Bacon, J. C. Bardin, R. Barends, R. Biswas, S. Boixo, F. G. Brandao, D. A. Buell, et al., *Nature* **574**, 505 (2019).
- [2] S. Boixo, S. V. Isakov, V. N. Smelyanskiy, R. Babbush, N. Ding, Z. Jiang, M. J. Bremner, J. M. Martinis, and H. Neven, *Nature Physics* **14**, 595 (2018).
- [3] A. W. Cross, L. S. Bishop, S. Sheldon, P. D. Nation, and J. M. Gambetta, *Physical Review A* **100**, 032328 (2019).
- [4] M. Cramer, M. B. Plenio, S. T. Flammia, R. Somma, D. Gross, S. D. Bartlett, O. Landon-Cardinal, D. Poulin, and Y.-K. Liu, *Nature communications* **1**, 149 (2010).
- [5] B. Lanyon, C. Maier, M. Holzäpfel, T. Baumgratz, C. Hempel, P. Jurcevic, I. Dhand, A. Buyskikh, A. Daley, M. Cramer, et al., *Nature Physics* **13**, 1158 (2017).
- [6] R. O'Donnell and J. Wright, in *Proceedings of the forty-eighth annual ACM symposium on Theory of Computing* (2016), pp. 899–912.
- [7] D. Gross, Y.-K. Liu, S. T. Flammia, S. Becker, and J. Eisert, *Physical review letters* **105**, 150401 (2010).
- [8] E. Knill, D. Leibfried, R. Reichle, J. Britton, R. B. Blakestad, J. D. Jost, C. Langer, R. Ozeri, S. Seidelin, and D. J. Wineland, *Physical Review A* **77**, 012307 (2008).
- [9] E. Magesan, J. M. Gambetta, and J. Emerson, *Physical review letters* **106**, 180504 (2011).
- [10] E. Magesan, J. M. Gambetta, and J. Emerson, *Physical Review A* **85**, 042311 (2012).
- [11] A. Erhard, J. J. Wallman, L. Postler, M. Meth, R. Stricker, E. A. Martinez, P. Schindler, T. Monz, J. Emerson, and R. Blatt, *Nature communications* **10**, 5347 (2019).
- [12] R. Harper, S. T. Flammia, and J. J. Wallman, *Nature Physics* **16**, 1184 (2020).
- [13] S. T. Flammia and J. J. Wallman, *ACM Transactions on Quantum Computing* **1**, 1 (2020).
- [14] C. Bădescu, R. O'Donnell, and J. Wright, in *Proceedings of the 51st Annual ACM SIGACT Symposium on Theory of Computing* (2019), pp. 503–514.
- [15] J. Eisert, D. Hangleiter, N. Walk, I. Roth, D. Markham, R. Parekh, U. Chabaud, and E. Kashefi, *Nature Reviews Physics* **2**, 382 (2020).
- [16] K. Bharti, A. Cervera-Lierta, T. H. Kyaw, T. Haug, S. Alperin-Lea, A. Anand, M. Degroote, H. Heimonen, J. S. Kottmann, T. Menke, et al., *Reviews of Modern Physics* **94**, 015004 (2022).
- [17] J. P. Gaebler, A. M. Meier, T. R. Tan, R. Bowler, Y. Lin, D. Hanneke, J. D. Jost, J. Home, E. Knill, D. Leibfried, et al., *Physical review letters* **108**, 260503 (2012).
- [18] J. Wallman, C. Granade, R. Harper, and S. T. Flammia, *New Journal of Physics* **17**, 113020 (2015).
- [19] J. J. Wallman, *Quantum* **2**, 47 (2018).
- [20] T. J. Proctor, A. Carignan-Dugas, K. Rudinger, E. Nielsen, R. Blume-Kohout, and K. Young, *Physical review letters* **123**, 030503 (2019).
- [21] J. Helsen, X. Xue, L. M. Vandersypen, and S. Wehner, *npj Quantum Information* **5**, 71 (2019).
- [22] J. Chen, D. Ding, and C. Huang, *PRX Quantum* **3**, 030320 (2022).
- [23] T. Proctor, S. Seritan, K. Rudinger, E. Nielsen, R. Blume-Kohout, and K. Young, *Physical Review Letters* **129**, 150502 (2022).
- [24] J. Hines, M. Lu, R. K. Naik, A. Hashim, J.-L. Ville, B. Mitchell, J. M. Kriekebaum, D. I. Santiago, S. Seritan, E. Nielsen, et al., *Physical Review X* **13**, 041030 (2023).
- [25] T. Proctor, K. Rudinger, K. Young, E. Nielsen, and R. Blume-Kohout, *Nature Physics* **18**, 75 (2022).
- [26] M. Sarovar, T. Proctor, K. Rudinger, K. Young, E. Nielsen, and R. Blume-Kohout, *Quantum* **4**, 321 (2020).
- [27] S. Krinner, S. Lazar, A. Remm, C. K. Andersen, N. Lacroix, G. J. Norris, C. Hellings, M. Gabureac, C. Eichler, and A. Wallraff, *Physical Review Applied* **14**, 024042 (2020).
- [28] K. Rudinger, C. W. Hogle, R. K. Naik, A. Hashim, D. Lobser, D. I. Santiago, M. D. Grace, E. Nielsen, T. Proctor, S. Seritan, et al., *PRX Quantum* **2**, 040338 (2021).
- [29] Y. Sung, L. Ding, J. Braumüller, A. Vepsäläinen, B. Kannan, M. Kjaergaard, A. Greene, G. O. Samach, C. McNally, D. Kim, et al., *Physical Review X* **11**, 021058 (2021).
- [30] A. Kandala, K. X. Wei, S. Srinivasan, E. Magesan, S. Carnevale, G. Keefe, D. Klaus, O. Dial, and D. McKay, *Physical Review Letters* **127**, 130501 (2021).
- [31] A. Elben, S. T. Flammia, H.-Y. Huang, R. Kueng, J. Preskill, B. Vermersch, and P. Zoller, *Nature Reviews Physics* **5**, 9 (2023).
- [32] J. J. Wallman and J. Emerson, *Physical Review A* **94**, 052325 (2016).
- [33] M. A. Nielsen and I. Chuang, *Quantum computation and quantum information* (American Association of Physics Teachers, 2002).
- [34] E. Magesan, J. M. Gambetta, B. R. Johnson, C. A. Ryan, J. M. Chow, S. T. Merkel, M. P. Da Silva, G. A. Keefe, M. B. Rothwell, T. A. Ohki, et al., *Physical review letters* **109**, 080505 (2012).
- [35] E. Onorati, A. Werner, and J. Eisert, *Physical review letters* **123**, 060501 (2019).
- [36] T. Proctor, S. Seritan, E. Nielsen, K. Rudinger, K. Young, R. Blume-Kohout, and M. Sarovar, arXiv preprint arXiv:2204.07568 (2022).
- [37] A. Carignan-Dugas, D. Dahlen, I. Hincks, E. Ospadov, S. J. Beale, S. Ferracin, J. Skanes-Norman, J. Emerson, and J. J. Wallman, arXiv preprint arXiv:2303.17714 (2023).

- [38] Y. Gu, W.-F. Zhuang, X. Chai, and D. E. Liu, arXiv preprint arXiv:2301.02056 (2023).
 [39] A. Carignan-Dugas, S. K. Ranu, and P. Dreher, arXiv preprint arXiv:2303.09945 (2023).
 [40] J. A. Gyamfi, European Journal of Physics **41**, 063002 (2020).
 [41] S. Blanes, F. Casas, J.-A. Oteo, and J. Ros, Physics reports **470**, 151 (2009).
 [42] I. Henao, J. P. Santos, and R. Uzdin, arXiv preprint arXiv:2303.05001 (2023).
 [43] T. Alexander, N. Kanazawa, D. J. Egger, L. Capelluto, C. J. Wood, A. Javadi-Abhari, and D. C. McKay, Quantum Science and Technology **5**, 044006 (2020).
 [44] T. Proctor, K. Rudinger, K. Young, M. Sarovar, and R. Blume-Kohout, Physical review letters **119**, 130502 (2017).
 [45] F. B. Maciejewski, Z. Zimborás, and M. Oszmaniec, Quantum **4**, 257 (2020).
 [46] P. D. Nation, H. Kang, N. Sundaresan, and J. M. Gambetta, PRX Quantum **2**, 040326 (2021).
 [47] H. Landa, D. Meiroum, N. Kanazawa, M. Fitzpatrick, and C. J. Wood, Physical Review Research **4**, 013199 (2022).
 [48] S. Endo, Z. Cai, S. C. Benjamin, and X. Yuan, Journal of the Physical Society of Japan **90**, 032001 (2021).
 [49] R. Barends, J. Kelly, A. Megrant, A. Veitia, D. Sank, E. Jeffrey, T. C. White, J. Mutus, A. G. Fowler, B. Campbell, et al., Nature **508**, 500 (2014).

APPENDIX I - APPROXIMATE EVOLUTIONS USING THE MAGNUS EXPANSION

In this appendix, we derive the approximations given in Eqs. (8) and (13). Let us start with the operator \tilde{K} , which represents the solution to the equation

$$d_t|\rho\rangle\rangle = (-iH_L(t) + \mathcal{L}(t))|\rho\rangle\rangle. \quad (51)$$

Using the solution $U_L(t)$ to the error-free equation $d_t|\rho\rangle\rangle = -iH_L(t)|\rho\rangle\rangle$, we define the interaction picture vector

$$|\rho_{int}\rangle\rangle = U_L^\dagger(t)|\rho\rangle\rangle. \quad (52)$$

In this way, Eq. (51) can be rewritten in the interaction picture as

$$d_t|\rho_{int}\rangle\rangle = \mathcal{L}^{int}(t)|\rho_{int}\rangle\rangle, \quad (53)$$

where $\mathcal{L}^{int}(t) = U_L^\dagger(t)\mathcal{L}(t)U_L(t)$. The general solution to this equation can be expressed using the Magnus expansion [41]. Using this approach, the state $|\rho_{int}(T)\rangle\rangle$ at time T reads

$$|\rho_{int}(T)\rangle\rangle = e^{\Omega(T)}|\rho_{int}(0)\rangle\rangle, \quad (54)$$

where $\Omega(T) = \sum_{i=1}^{\infty} \Omega_i(T)$ is the Magnus expansion. The Magnus expansion is applicable to the general differential equation $d_t|\rho_{int}\rangle\rangle = \Lambda(t)|\rho_{int}\rangle\rangle$, with the operators $\Omega_i(T)$ expressed in terms of the operator $\Lambda(t)$. For $\Lambda(t) = \mathcal{L}^{int}(t)$, the first two terms $\Omega_1(T)$ and $\Omega_2(T)$ are given by

$$\Omega_1(T) = \int_0^T dt \mathcal{L}^{int}(t), \quad (55)$$

$$\Omega_2(T) = \frac{1}{2} \int_0^T dt' \int_0^{t'} [\mathcal{L}^{int}(t'), \mathcal{L}^{int}(t)] dt. \quad (56)$$

By multiplying both sides of Eq. (54) by $U_L(T)$, we obtain

$$|\rho(T)\rangle\rangle = U_L(T)e^{\Omega(T)}|\rho_0\rangle\rangle, \quad (57)$$

where $|\rho_0\rangle\rangle = |\rho_{int}(0)\rangle\rangle$ is the initial state in the Schrodinger picture. Thus, Eq. (8) is the result of approximating the exact solution $\tilde{K} := U_L(T)e^{\Omega(T)}$, by discarding the Magnus terms $\Omega_{i \geq 2}(T)$. We also point out that in the main text we write $\Omega_1(T)$ as Ω_1 .

For the operator $K_I K$, we must find the solution to the equation

$$d_t|\rho\rangle\rangle = (-iH_{L,\text{ext}}(t) + \mathcal{L}'_{\text{ext}}(t))|\rho\rangle\rangle, \quad (58)$$

where

$$H_{L,\text{ext}}(t) = \begin{cases} H_L(t), & \text{for } t \in (0, T), \\ H_I(t-T) \otimes I - I \otimes H_I^\dagger(t-T), & \text{for } t \in (T, 2T), \end{cases} \quad (59)$$

and

$$\mathcal{L}'_{\text{ext}}(t) = \begin{cases} \mathcal{L}'(t), & \text{for } t \in (0, T), \\ -i\delta H_L(t) + \mathcal{L}_I(t-T), & \text{for } t \in (T, 2T). \end{cases} \quad (60)$$

We note that Eq. (58) is an extension of Eq. (5) to the total time interval $(T, 2T)$. For $t \in (T, 2T)$, $H_{L,\text{ext}}(t)$ and $\mathcal{L}'_{\text{ext}}(t)$ are defined according to the prescriptions given in Sec. IVB of the main text. Here, $\mathcal{L}'(t) = -i\delta H_L(t) + \mathcal{L}(t)$ (cf. Eq. (5)). We further remark that since we consider general coherent errors in the time domains $(0, T)$ and $(T, 2T)$, the notation $\delta H_L(t)$ can be extended to $(T, 2T)$ without risk of confusion.

Since Eq. (58) is also of the general form $d_t|\rho_{\text{int}}\rangle\rangle = \Lambda(t)|\rho_{\text{int}}\rangle\rangle$, we can resort to the Magnus expansion to express its solution. The interaction picture vector $|\rho_{\text{int}}\rangle\rangle$ for $t \in (0, T)$ is defined through Eq. (52). For $t \in (T, 2T)$, we must consider the ideal evolution associated with this interval. To obtain the corresponding unitary, let us first consider the evolution $U_I(t)$ generated by the driving $H_I(t)$. For $t \in (0, T)$, $H_I(t)$ is such that it undoes the portion of the $U(T)$ generated in the time subinterval $(T-t, T)$. That is, $U_I(t)U(T) = U(T-t)$. Expressing this relationship in the interval $(T, 2T)$ involves the time shift $t \rightarrow t-T$, which leads to $U(T-t) \rightarrow U(2T-t)$. Similarly, in Liouville space $U_L(T-t) \rightarrow U_L(2T-t)$. Therefore,

$$|\rho_{\text{int}}\rangle\rangle = \begin{cases} U_L^\dagger(t)|\rho\rangle\rangle, & \text{for } t \in (0, T), \\ U_L^\dagger(2T-t)|\rho\rangle\rangle, & \text{for } t \in (T, 2T). \end{cases} \quad (61)$$

We stress that none of the derivations in this appendix or the rest of the present article assume some special structure of the Hamiltonian. The time dependence of $H(t)$ is general and commutativity at different times is not required. However, it is also important to keep in mind that $H_I(t)$ is by construction related to $H(t)$. Thus, the evolution can be arbitrary in the time interval $t \in (0, T)$, but not in the total interval $t \in (0, 2T)$.

Using Eq. (61), the dynamical equation (58) in the interaction picture reads

$$d_t|\rho_{\text{int}}\rangle\rangle = (\mathcal{L}'_{\text{ext}})^{\text{int}}(t)|\rho_{\text{int}}\rangle\rangle, \quad (62)$$

where

$$(\mathcal{L}'_{\text{ext}})^{\text{int}}(t) = \begin{cases} U_L^\dagger(t)\mathcal{L}'_{\text{ext}}U_L(t), & \text{for } t \in (0, T), \\ U_L^\dagger(2T-t)\mathcal{L}'_{\text{ext}}U_L(2T-t), & \text{for } t \in (T, 2T). \end{cases} \quad (63)$$

The first Magnus term for $K_I K$ is obtained by integrating $(\mathcal{L}'_{\text{ext}})^{\text{int}}$ from $t=0$ to $t=2T$, and is given by

$$\begin{aligned} \Omega_1(2T) &= \int_0^{2T} dt (\mathcal{L}'_{\text{ext}})^{\text{int}}(t) \\ &= \int_0^T dt U_L^\dagger(t)\mathcal{L}'_{\text{ext}}(t)U_L(t) + \int_T^{2T} dt U_L^\dagger(2T-t)\mathcal{L}'_{\text{ext}}(t)U_L(2T-t). \end{aligned} \quad (64)$$

In contrast with Eq. (54), $(\mathcal{L}'_{\text{ext}})^{\text{int}}(t)$ contains not only the contribution from noise, embodied by the dissipators $\mathcal{L}(t)$ and $\mathcal{L}_I(t-T)$, but also the coherent errors $\delta H_L(t)$. The total coherent error in $\Omega_1(2T)$ is $-i\Theta$, with Θ expressed by Eq. (14). Regarding the noise, we have the sum of the two terms $\int_0^T dt U_L^\dagger(t)\mathcal{L}(t)U_L(t)$ and $\int_T^{2T} dt U_L^\dagger(2T-t)\mathcal{L}_I(t-T)U_L(2T-t)$. Since $\mathcal{L}_I(t-T) = \mathcal{L}(2T-t)$ (cf. Eq. (18)), we can perform the change of variable $t' = 2T-t$, to obtain

$$\int_T^{2T} dt U_L^\dagger(2T-t)\mathcal{L}_I(t-T)U_L(2T-t) = \int_0^T dt' U_L^\dagger(t')\mathcal{L}(t')U_L(t'). \quad (65)$$

Therefore, the noisy component of $\Omega_1(2T)$ is given by $2 \int_0^T dt U_L^\dagger(t)\mathcal{L}(t)U_L(t) = 2\Omega_1(T)$. This leads us to conclude that $K_I K \approx e^{2\Omega_1 - i\Theta}$.

APPENDIX II - PROOF OF THE PROPERTY $\langle\langle\rho_0|\Theta|\rho_0\rangle\rangle = 0$

From the definition of Θ (cf. Eq. (14)), we have that

$$\langle\langle\rho_0|\Theta|\rho_0\rangle\rangle = \int_0^T \langle\langle\rho(t)|\delta H_L(t)|\rho(t)\rangle\rangle dt + \int_T^{2T} \langle\langle\rho(2T-t)|\delta H_L(t)|\rho(2T-t)\rangle\rangle dt, \quad (66)$$

where $|\rho(t)\rangle\rangle = U_L(t)|\rho_0\rangle\rangle$. The Hamiltonian deviation $\delta H_L(t)$ in Liouville space is related to a Hamiltonian deviation $\delta H(t)$ in Hilbert space. That is, $\delta H_L(t) = \delta H(t) \otimes I - I \otimes \delta H(t)^T$, in such a way that the total Hamiltonian in Hilbert space reads $H(t) + \delta H(t)$. This implies that in Hilbert space the vector $\delta H_L(t)|\rho(t)\rangle\rangle$ takes the form $[\delta H(t), \rho(t)]$ or, equivalently,

$$\delta H_L(t)|\rho(t)\rangle\rangle = |[\delta H(t), \rho(t)]\rangle\rangle, \quad (67)$$

where $|A\rangle\rangle$ denotes a column vector associated with an arbitrary matrix A of dimension $n \times n$.

Accordingly, we can write $\langle\langle\rho(t)|\delta H_L(t)|\rho(t)\rangle\rangle$ as

$$\langle\langle\rho(t)|\delta H_L(t)|\rho(t)\rangle\rangle = \langle\langle\rho(t)|[\delta H(t), \rho(t)]\rangle\rangle. \quad (68)$$

By applying Eq. (4) to the right hand side of (68), it follows that

$$\begin{aligned} \langle\langle\rho(t)|\delta H_L(t)|\rho(t)\rangle\rangle &= \text{Tr}(\rho^\dagger(t)[\delta H(t), \rho(t)]) \\ &= \text{Tr}(\rho(t)\delta H(t)\rho(t) - \rho(t)\rho(t)\delta H(t)) \\ &= 0, \end{aligned} \quad (69)$$

where in the second we apply the hermiticity of $\rho(t)$, and the cyclic property of the trace is used in the third line. Since this is equally valid if we replace $\rho(t)$ by any hermitian operator, we conclude that $\langle\langle\rho_0|\Theta|\rho_0\rangle\rangle = 0$.

APPENDIX III - ROBUSTNESS TO SPAM ERRORS

Here, we characterize SPAM errors and show that the estimation of σ_n is robust to leading corrections associated with these errors. We start by deriving Eqs. (35) and (36). Equation (35) follows by applying once again the Magnus expansion to $d_t|\rho_{int}\rangle\rangle = \Lambda_p(t)|\rho_{int}\rangle\rangle$, where $\Lambda_p(t)$ contains the dissipator and the Hamiltonian deviation (coherent errors) that affect the implementation of U_p , written in the interaction picture. Moreover, $|\rho_{int}\rangle\rangle$ is defined similarly to Eq. (52), with $U_L(t)$ replaced by the (error-free) preparation unitary evaluated at time t . The initial erroneous state is thus given by $U_p e^{\Omega_p} |0\rangle\rangle$, being $\Omega_p = \sum_{i=1}^{\infty} \Omega_{p,i}$ the Magnus expansion that accounts for preparation errors. In particular,

$$\Omega_{p,1} = \int_0^{T_p} dt \Lambda_p(t), \quad (70)$$

$$\Omega_{p,2} = \frac{1}{2} \int_0^{T_p} dt' \int_0^{t'} [\Lambda_p(t'), \Lambda_p(t)] dt, \quad (71)$$

where T_p is the time invested in the preparation stage.

For the measurement stage, the target circuit is U_p^\dagger . The error-prone dynamics yields an imperfect implementation $K_m = U_p^\dagger e^{\Omega_m}$ of U_p^\dagger , with a Magnus expansion Ω_m that in general differs from Ω_p . In contrast with Eq. (36), in the previous expression for K_m the ideal unitary U_p^\dagger appears at the l.h.s. of e^{Ω_m} . The first step to address this issue is to realize that we can express K_m as $K_m = (U_p^\dagger e^{\Omega_m} U_p) U_p^\dagger$. Since $(U_p^\dagger \Omega_m U_p)^n = U_p^\dagger \Omega_m^n U_p$ for any positive integer n , the unitaries U_p^\dagger and U_p can be absorbed into the the exponent of K_m , i.e. $U_p^\dagger e^{\Omega_m} U_p = e^{U_p^\dagger \Omega_m U_p} := e^{\bar{\Omega}_m}$. Therefore, $K_m = e^{\bar{\Omega}_m} U_p^\dagger$, in agreement with Eq. (36).

Now, let us characterize the corrections to σ_n that result from SPAM errors. We recall that these errors impact the measurement of the quantities $R_k = \langle\langle\rho_0|e^{kX}|\rho_0\rangle\rangle = \langle\langle 0|U_p^\dagger e^{kX} U_p|0\rangle\rangle$, due to the non-ideal implementations of

U_p and U_p^\dagger . Thus, instead of R_k what is measured in practice is $R'_k = \langle\langle \rho_m | e^{k\chi} | \rho_p \rangle\rangle$, where $|\rho_p\rangle\rangle = U_p e^{\Omega_p} |0\rangle\rangle$ and $\langle\langle \rho_m | = \langle\langle 0 | e^{\bar{\Omega}_m} U_p^\dagger$. This also substitutes the SPAM-free quantity $\sigma_n = \sum_{k=0}^n a_k^{(n)} R_k$ by $\sigma'_n = \sum_{k=0}^n a_k^{(n)} R'_k$.

Our goal is to show that SPAM errors that dominate each term R'_k are suppressed in the calculation of σ'_n . As we shall see, the key property behind this suppression is the condition (cf. Eq. (26) for $j=0$)

$$\sum_{k=0}^n a_k^{(n)} = 0. \quad (72)$$

By applying Eq. (72), we have that

$$\begin{aligned} \sigma'_n &= \sum_{k=1}^n a_k^{(n)} \{R'_k - R'_0\} \\ &= \sum_{k=1}^n a_k^{(n)} \{ \langle\langle \rho_m | e^{k\chi} | \rho_p \rangle\rangle - \langle\langle \rho_m | \rho_p \rangle\rangle \} \\ &= \sum_{k=1}^n a_k^{(n)} \langle\langle 0 | \{ e^{\bar{\Omega}_m} U_p^\dagger e^{k\chi} U_p e^{\Omega_p} - e^{\bar{\Omega}_m} e^{\Omega_p} \} | 0 \rangle\rangle. \end{aligned} \quad (73)$$

In addition, for each $0 \leq k \leq n$ we can expand the exponentials in the last line of Eq. (73) to obtain

$$\begin{aligned} e^{\bar{\Omega}_m} U_p^\dagger e^{k\chi} U_p e^{\Omega_p} - e^{\bar{\Omega}_m} e^{\Omega_p} &= e^{\bar{\Omega}_m} U_p^\dagger \sum_{l=1}^{\infty} (k\chi)^l U_p e^{\Omega_p} \\ &= U_p^\dagger \sum_{l=1}^{\infty} (k\chi)^l U_p + \sum_{l=1}^{\infty} k^l \bar{\chi}^l \sum_{l'=1}^{\infty} \Omega_p^{l'} \\ &\quad + \sum_{l=1}^{\infty} \bar{\Omega}_m^l \sum_{l'=1}^{\infty} k^l \bar{\chi}^{l'} + \sum_{l=1}^{\infty} \bar{\Omega}_m^l \sum_{l'=1}^{\infty} k^l \bar{\chi}^{l'} \sum_{l''=1}^{\infty} \Omega_p^{l''}, \end{aligned} \quad (74)$$

where $\bar{\chi} := U_p^\dagger \chi U_p$.

The first term in the second line of Eq. (74) can be rewritten as $U_p^\dagger e^{k\chi} U_p - I_L$. Therefore, its contribution to σ'_n is given by

$$\begin{aligned} \sum_{k=1}^n a_k^{(n)} \langle\langle 0 | \{ U_p^\dagger e^{k\chi} U_p - I_L \} | 0 \rangle\rangle &= \sum_{k=1}^n a_k^{(n)} \{ \langle\langle \rho_0 | e^{k\chi} | \rho_0 \rangle\rangle - \langle\langle \rho_0 | \rho_0 \rangle\rangle \} \\ &= \sigma_n, \end{aligned} \quad (75)$$

while the remaining terms provide corrections to σ_n . According to Eq. (74), the leading-order terms in the difference $\sigma'_n - \sigma_n$ are $\langle\langle 0 | \bar{\chi} \Omega_p | 0 \rangle\rangle$ and $\langle\langle 0 | \bar{\Omega}_m \bar{\chi} | 0 \rangle\rangle$, which constitute quadratic corrections to σ_n . Hence, σ'_n is robust to the leading (linear) corrections that appear in each R'_k . For example, R'_1 is affected by the linear error terms $\langle\langle 0 | \bar{\chi} | 0 \rangle\rangle$, $\langle\langle 0 | \Omega_p | 0 \rangle\rangle$, and $\langle\langle 0 | \bar{\Omega}_m | 0 \rangle\rangle$. We also remark that the SPAM contributions $\langle\langle 0 | \sum_{l=1}^{\infty} \Omega_p^l | 0 \rangle\rangle$, $\langle\langle 0 | \sum_{l=1}^{\infty} \bar{\Omega}_m^l | 0 \rangle\rangle$, and $\langle\langle 0 | \sum_{l=1}^{\infty} \Omega_p^l \sum_{l'=1}^{\infty} \bar{\Omega}_m^{l'} | 0 \rangle\rangle$, characteristic of each R'_k , are absent in σ'_n .

Taking into account Eqs. (74) and (75), the application of the triangular inequality yields

$$\begin{aligned} |\sigma'_n - \sigma_n| &\leq \sum_{k=1}^n |a_k^{(n)}| \left\{ \sum_{l,l'=1}^{\infty} k^l \left| \langle\langle 0 | \bar{\chi}^l \Omega_p^{l'} | 0 \rangle\rangle \right| + \sum_{l,l'=1}^{\infty} k^l \left| \langle\langle 0 | \bar{\Omega}_m^l \bar{\chi}^{l'} | 0 \rangle\rangle \right| \right. \\ &\quad \left. + \sum_{l,l',l''=1}^{\infty} k^l \left| \langle\langle 0 | \bar{\Omega}_m^l \bar{\chi}^{l'} \Omega_p^{l''} | 0 \rangle\rangle \right| \right\}. \end{aligned} \quad (76)$$

In addition, the definition of the spectral norm $\|*\|$ and the fact that $\langle\langle 0 | 0 \rangle\rangle = 1$ allows us to bound each term in Eq. (76). For example, for the leading order terms we have that

$$|\langle\langle 0|\bar{\chi}\Omega_p|0\rangle\rangle| \leq \|\bar{\chi}\Omega_p\| \leq \|\chi\| \|\Omega_p\|, \quad (77)$$

$$|\langle\langle 0|\bar{\Omega}_m\bar{\chi}|0\rangle\rangle| \leq \|\bar{\Omega}_m\bar{\chi}\| \leq \|\Omega_m\| \|\chi\|, \quad (78)$$

where the definition of $\|\cdot\|$ is used in the middle inequalities, and the rightmost inequalities follow from the submultiplicativity of $\|\cdot\|$ and its unitary invariance. From Eq. (76), it is also clear that a generic term at the r.h.s. has an upper bound proportional to $\|\Omega_m\|^{l'} \|\chi\|^l \|\Omega_p\|^{l''}$, with $l' + l'' \geq 1$ and $l \geq 1$.

APPENDIX IV - MITIGATION OF LOCAL READOUT ERRORS

Readout errors lead to incorrect measurements in quantum computing. Usually, these measurements are projective measurements in the computational basis, and determine the state of each qubit as being “0” or “1”. A readout error occurs when the true state is 0 and it is registered as 1 or vice versa. In a system composed of N qubits, it is possible to characterize readout errors by using a $2^N \times 2^N$ “detector matrix” \mathbf{D} . An element $\mathbf{D}_{i,j}$ of this matrix represents the probability of measuring the (N -qubit) computational state i , given that the true state is j .

Suppose now that we perform a measurement after implementing some generic quantum circuit. If q_i denotes the probability of measuring the computational state i , in the presence of readout errors, the probability vector $\mathbf{q} = (q_1, q_2, \dots, q_{2^N})^T$ can be written as

$$\mathbf{q} = \mathbf{D}\mathbf{p}, \quad (79)$$

where $\mathbf{p} = (p_1, p_2, \dots, p_{2^N})^T$ and p_i is the probability for measuring i in the absence of readout errors. Thus, the “error-free” (note that the probabilities p_i can include preparation errors and circuit errors but by definition they exclude readout errors) probabilities \mathbf{p} are given by

$$\mathbf{p} = \mathbf{D}^{-1}\mathbf{q}. \quad (80)$$

A column $\{\mathbf{D}_{i,j}\}_i$ of the detector matrix \mathbf{D} can be experimentally determined by preparing the computational state j and measuring the corresponding probability distribution. If N is small, the full matrix \mathbf{D} can be constructed from the measurements performed on all the computational states. However, such a procedure is not scalable because there are 2^N computational states. On the other hand, one can model the readout errors by assuming that they contain negligible correlations. If this assumption is well founded, the matrix \mathbf{D} takes the form of a tensor product

$$\mathbf{D} = \mathbf{D}_1 \otimes \mathbf{D}_2 \otimes \dots \otimes \mathbf{D}_k \otimes \dots, \quad (81)$$

where the matrices \mathbf{D}_k represent local detector matrices acting on subsets of qubits. In this case, it is possible to efficiently determine the matrix \mathbf{D} , if all the matrices \mathbf{D}_k have small dimension and this dimension is independent of N . For example, completely uncorrelated readout errors would be characterized by measuring N single-qubit detector matrices. The mitigation of local readout errors is performed through the inverse

$$\mathbf{D}^{-1} = \mathbf{D}_1^{-1} \otimes \mathbf{D}_2^{-1} \otimes \dots \otimes \mathbf{D}_k^{-1} \otimes \dots, \quad (82)$$

which can also be efficiently computed for local detector matrices of small dimension.

For completely uncorrelated readout errors, preparing the two computational states where all the qubits are in the ground (“0”) state or all the qubits are in the excited (“1”) state is sufficient to evaluate \mathbf{D} . This procedure is equivalent to a simultaneous preparation of all the qubits in any of its two computational states. Thus, the associated readout statistics provides all the information required to determine the local detector matrices \mathbf{D}_k .

APPENDIX V - DESCRIPTION OF ERROR SOURCES IN NUMERICAL SIMULATIONS

In this appendix, we provide a detailed description of the error models used for the simulations of Sec. V. First, we will characterize the error sources associated with the simulation of the GHZ state, and then the error sources simulated in the calculation of the average incoherent infidelity. In both cases the CNOT gates are based on the cross resonance interaction (cf. Eq. (40)).

Error sources for the simulation of the GHZ state

We assume that two-qubit gates are the only gates affected by noise. More specifically, we consider local dephasing and amplitude damping that act alongside the cross resonance pulse used for the implementation of CNOT gates. In the case of the circuit used for preparing the five-qubit GHZ state, these noise channels operate on all the qubits of the quantum register and not only on the specific pair that undergoes the cross resonance interaction. The corresponding error-free evolution is given by

$$U_{GHZ} = U_{CNOT}^{(4,5)} U_{CNOT}^{(3,4)} U_{CNOT}^{(2,3)} U_{CNOT}^{(1,2)} U_{had}^{(1)}, \quad (83)$$

where $U_{had}^{(1)}$ represents a Hadamard gate acting on qubit 1. We also remark that in Eq. (83) we use the standard notation for unitary operators that act on density matrices. In particular, the associated CNOT gates obey Eq. (40).

The effect of noise is introduced through the superoperators

$$\hat{D}[\rho] = \sum_{i=1}^5 \left\{ Z_i \rho Z_i^\dagger - \frac{1}{2} Z_i^\dagger Z_i \rho - \frac{1}{2} \rho Z_i^\dagger Z_i \right\}, \quad (84)$$

$$\hat{A}[\rho] = \sum_{i=1}^5 \left\{ \sigma_-^{(i)} \rho \sigma_+^{(i)} - \frac{1}{2} \sigma_+^{(i)} \sigma_-^{(i)} \rho - \frac{1}{2} \rho \sigma_+^{(i)} \sigma_-^{(i)} \right\}, \quad (85)$$

where \hat{D} stands for dephasing, \hat{A} stands for amplitude damping, and $\sigma_-^{(i)}$ is the annihilation operator $\begin{pmatrix} 0 & 1 \\ 0 & 0 \end{pmatrix}$ acting on the qubit i (in addition, $\sigma_+^{(i)} = \sigma_-^{(i)\dagger}$). By adding Eqs. (84) and (85) to the unitary dynamics generated by the cross resonance Hamiltonian $Z_j \otimes X_k$ (which includes also the contribution from coherent errors), we obtain a GKLS (Gorini-Kossakowski-Sudarshan-Lindblad) master equation for the error-prone evolution. We consider equal relaxation rates for \hat{D} and \hat{A} , which leads to the total noise superoperator

$$\hat{L}[\rho] = \xi \left\{ \frac{1}{2} \hat{D}[\rho] + \frac{1}{2} \hat{A}[\rho] \right\}. \quad (86)$$

The parameter ξ characterizes the strength of the noise. Moreover, \hat{L} generates the dissipator \mathcal{L} in the Liouville space formalism, as described below.

For the Liouville space representation of the noise channels \hat{D} and \hat{A} , we use the calligraphic letters \mathcal{D} and \mathcal{A} , respectively. In this representation, such superoperators become $N^2 \times N^2 = 2^{10} \times 2^{10}$ matrices given by [40]

$$\mathcal{D} = \sum_{i=1}^5 \{ Z_i \otimes Z_i - I_L \}, \quad (87)$$

$$\mathcal{A} = \sum_{i=1}^5 \left\{ \sigma_i^{(-)} \otimes \sigma_i^{(-)} - \frac{1}{2} \sigma_i^{(+)} \sigma_i^{(-)} \otimes I - \frac{1}{2} I \otimes \sigma_i^{(+)} \sigma_i^{(-)} \right\}. \quad (88)$$

Importantly, each matrix labeled by i in Eqs. (87) and (88) is an $N \times N$ matrix that includes an implicit tensor product with a $2^4 \times 2^4$ identity matrix, acting on all the qubits different from i . The corresponding dissipator reads

$$\mathcal{L} = \xi \left\{ \frac{1}{2} \mathcal{D} + \frac{1}{2} \mathcal{A} \right\}. \quad (89)$$

Since the Hamiltonian $Z_j \otimes X_k$ is time independent, and noise is only active during the cross resonance pulse, \mathcal{L} retains also its time independence.

Therefore, the error-prone implementation of $U_{CNOT}^{(j,k)}$ is governed by the master equation

$$d_t |\rho\rangle = \left(-i H_L^{(j,k)} - i \delta H_L^{(j,k)} + \mathcal{L} \right) |\rho\rangle, \quad (90)$$

$$H_L^{(j,k)} = (Z_j \otimes X_k) \otimes I - I \otimes (Z_j \otimes X_k)^T, \quad (91)$$

$$\delta H_L^{(j,k)} = \eta \left\{ (Z_j \otimes Z_k) \otimes I - I \otimes (Z_j \otimes Z_k)^T \right\}, \quad (92)$$

where \mathcal{L} is given by Eq. (89). In Eqs. (91) and (92), it is important to stress that the terms $Z_j \otimes X_k$ and $Z_j \otimes Z_k$ are $N \times N$ matrices that act as the identity for all the qubits different from j and k . Equation (90) can be directly integrated to obtain the exact solution $e^{(-iH_L^{(j,k)}T - i\delta H_L^{(j,k)} + \mathcal{L})T}$, where T is the time invested in the cross resonance interaction.

In this simulation, we assume that all the single-qubit gates are error-free. Accordingly, the error-prone implementation of $U_{CNOT}^{(j,k)}$ is given by

$$K_{CNOT}^{(j,k)} = e^{i\frac{\pi}{4}X_k} \otimes e^{-i\frac{\pi}{4}X_k} K_{CR}^{(j,k)} e^{i\frac{\pi}{4}Z_j} \otimes e^{-i\frac{\pi}{4}Z_j}, \quad (93)$$

$$K_{CR}^{(j,k)} = e^{(-iH_L^{(j,k)} - i\delta H_L^{(j,k)} + \mathcal{L})T}, \quad (94)$$

where the rotations $e^{i\frac{\pi}{4}X_k}$ and $e^{i\frac{\pi}{4}Z_j}$ are expressed using the representation of unitary operators in Liouville space. Specifically, the matrix corresponding to a unitary U reads $U \otimes U^*$, where U^* is the elementwise complex conjugate of U . Since $U_{had}^{(1)}$ is a real matrix, the error-prone implementation of U_{GHZ} is given by

$$K = K_{CNOT}^{(4,5)} K_{CNOT}^{(3,4)} K_{CNOT}^{(2,3)} K_{CNOT}^{(1,2)} U_{had}^{(1)} \otimes U_{had}^{(1)}. \quad (95)$$

Let us now characterize the inverse evolution K_I , following the pulse inverse approach on which our theory is based. Due to the time independence of $Z_j \otimes X_k$, the driving that reverses the corresponding CNOT in the error-free scenario is simply $-Z_j \otimes X_k$. Thus, the ideal inverse for this gate reads

$$U_{I,CNOT}^{(j,k)} = e^{-i\frac{\pi}{4}Z_j} U_{CR}^\dagger e^{-i\frac{\pi}{4}X_k}. \quad (96)$$

Since the dissipator remains invariant under a sign change of the Hamiltonian, in the error-prone execution of $U_{I,CNOT}^{(j,k)}$ noise is also characterized by Eq. (89). Furthermore, the parasitic term $Z_j \otimes Z_k$ is also unaffected by this sign reversal [27]. Accordingly, the implementation of $U_{I,CNOT}^{(j,k)}$ is given by

$$K_{I,CNOT}^{(j,k)} = e^{-i\frac{\pi}{4}Z_j} \otimes e^{i\frac{\pi}{4}Z_j} K_{I,CR}^{(j,k)} e^{-i\frac{\pi}{4}X_k} \otimes e^{i\frac{\pi}{4}X_k}, \quad (97)$$

where

$$K_{I,CR}^{(j,k)} = e^{(iH_L^{(j,k)} - i\delta H_L^{(j,k)} + \mathcal{L})T}. \quad (98)$$

This leads to the inverse evolution

$$K_I = U_{had}^{(1)} \otimes U_{had}^{(1)} K_{I,CNOT}^{(1,2)} K_{I,CNOT}^{(2,3)} K_{I,CNOT}^{(3,4)} K_{I,CNOT}^{(4,5)}. \quad (99)$$

For the sake of clarity, we remark that the exact infidelity $\varepsilon_{\text{inc}}(\varrho^{(\text{id})}, \tilde{\varrho})$ is computed with the final states

$$|\varrho^{(\text{id})}\rangle\rangle = U_{GHZ} \otimes U_{GHZ}^* |\rho_0\rangle\rangle, \quad (100)$$

$$|\tilde{\varrho}\rangle\rangle = \tilde{K} |\rho_0\rangle\rangle, \quad (101)$$

where \tilde{K} denotes the implementation of U_{GHZ} that excludes coherent errors. Specifically,

$$\tilde{K} = \tilde{K}_{CNOT}^{(4,5)} \tilde{K}_{CNOT}^{(3,4)} \tilde{K}_{CNOT}^{(2,3)} \tilde{K}_{CNOT}^{(1,2)} U_{had}^{(1)} \otimes U_{had}^{(1)}, \quad (102)$$

where $\tilde{K}_{CNOT}^{(j,k)} = e^{i\frac{\pi}{4}X_k} \otimes e^{-i\frac{\pi}{4}X_k} \left[e^{(-iH_L^{(j,k)} + \mathcal{L})T} \right] e^{i\frac{\pi}{4}Z_j} \otimes e^{-i\frac{\pi}{4}Z_j}$. Furthermore, the estimates of $\varepsilon_{\text{inc}}(\varrho^{(\text{id})}, \tilde{\varrho})$ through σ_n are evaluated with the evolutions K and K_I in Eqs. (95) and (99).

Error sources for the simulation of the average incoherent infidelity

In this example, we simulate the average incoherent infidelity of a CNOT gate, with respect to input states prepared by two-qubit Clifford gates. Any two-qubit Clifford gate can be obtained by combining single-qubit Clifford gates

with the CNOT gate, the SWAP gate, and the iSWAP gate (see Supplementary Information of [49]). Moreover, it is possible to implement the SWAP gate and the iSWAP gate using CNOT gates and single-qubit Clifford gates [49]. This implies that any two-qubit Clifford gate can be compiled using single-qubit Clifford gates and CNOT gates. Thus, our simulation of errors comprises noise and the $Z_1 \otimes Z_2$ coherent error, in the case of CNOT gates, and the single-qubit coherent errors described in Eqs. (43) and (44). These error sources affect both the target CNOT and the Clifford gates used for preparation and measurement. As in the previous example, we also introduce noise as local dephasing and amplitude damping acting alongside the cross resonance interaction. However, now we consider the dissipator

$$\mathcal{L} = \xi \left\{ \mathcal{D} + \frac{1}{10} \mathcal{A} \right\}, \quad (103)$$

which gives more weight to the dephasing channel \mathcal{D} . We also remark that for the channels \mathcal{D} and \mathcal{A} in Eq. (103) the summation limit in (87) and (88) must be replaced by 2.

In addition to the aforementioned error sources, we include readout errors and errors in the preparation of the fiducial state $|0\rangle\rangle$. Based on Reference [47], we consider a rotated fiducial state $|\hat{0}\rangle\rangle$, obtained by applying the rotation $R_Y(0.005\pi)R_X(0.005\pi)$ to the “0” state of each qubit. In this way, an initial state $|\rho_0^{(m)}\rangle\rangle$ is the result of applying an error-prone Clifford gate $K_p^{(m)}$ to $|\hat{0}\rangle\rangle$. That is,

$$|\rho_0^{(m)}\rangle\rangle = K_p^{(m)}|\hat{0}\rangle\rangle, \quad (104)$$

where the superscript m labels a gate randomly chosen from the set of two-qubit Clifford gates. The infidelities $\bar{\varepsilon}_{\text{inc}}$ and $\bar{\varepsilon}$ are thus computed using the final states $|\varrho^{(m)}\rangle\rangle = \tilde{K}|\rho_0^{(m)}\rangle\rangle$ and $|\varrho^{(m)}\rangle\rangle = K|\rho_0^{(m)}\rangle\rangle$, with $|\rho_0^{(m)}\rangle\rangle$ given in Eq. (104).

On the other hand, we incorporate single-qubit readout errors by using a noisy POVM (positive operator valued measurement) to characterize the corresponding measurement. This POVM has elements Π and $I_{2 \times 2} - \Pi$, where $I_{2 \times 2} = \begin{pmatrix} 1 & 0 \\ 0 & 1 \end{pmatrix}$ and [47]

$$\Pi = \sum_k \pi_k P_k, \quad P_k \in \{I_{2 \times 2}, X, Y, Z\}. \quad (105)$$

In the absence of readout errors, $\Pi = \frac{1}{2}(I_{2 \times 2} + Z) := \Pi^{(\text{id})}$ is the projector on the “0” state. This corresponds to $\pi_0 = \pi_3 = \frac{1}{2}$. For the noisy POVM, we consider the coefficients

$$\pi_0 = 0.501, \quad (106)$$

$$\pi_3 = 0.495, \quad (107)$$

$$\pi_1 = \pi_2 = 0. \quad (108)$$

In this way, the ideal row vector $\langle\langle 0| = \langle\langle \Pi_1^{(\text{id})} \otimes \Pi_2^{(\text{id})} |$ is substituted by $\langle\langle \Pi_{12} | := \langle\langle \Pi_1 \otimes \Pi_2 |$, where the subindices 1,2 label each qubit and both Π_1 and Π_2 are characterized by the coefficients (106)-(108). We note that the resulting POVM describes a small error affecting measurements in the computational basis. Specifically, the local detector matrix (see Appendix IV) is given by

$$\begin{aligned} \mathbf{D}_k &= \begin{pmatrix} \pi_0 + \pi_3 & \pi_0 - \pi_3 \\ 1 - (\pi_0 + \pi_3) & 1 - (\pi_0 - \pi_3) \end{pmatrix} \\ &= \begin{pmatrix} 0.996 & 0.006 \\ 0.004 & 0.994 \end{pmatrix}, \end{aligned} \quad (109)$$

where $k = 1, 2$.

For the m th Clifford gate, the n th-order estimation of the corresponding incoherent infidelity $\varepsilon_{\text{inc}}(\varrho_m^{(\text{id})}, \tilde{\varrho}_m)$ is performed through the quantity

$$\sigma_n^{(m)} = \sum_{k=0}^n a_k^{(n)} \langle\langle \Pi_{12} | K_m^{(m)} (K_I K)^k K_p^{(m)} |\hat{0}\rangle\rangle, \quad (110)$$

where $K_m^{(m)}$ is the error-prone Clifford gate used for the measurement. Therefore, we estimate the average incoherent infidelity using $-\frac{1}{2M} \sum_{m=1}^M \sigma_n^{(m)}$. The error-prone target evolution and its inverse are given by

$$K = e^{i\frac{\pi}{4}X_2} e^{i\theta Z_2} K_{CR}^{(1,2)} e^{i\frac{\pi}{4}Z_1}, \quad (111)$$

$$K_I = e^{-i\frac{\pi}{4}Z_1} K_{I,CR}^{(1,2)} e^{-i\theta Z_2} e^{-i\frac{\pi}{4}X_2}, \quad (112)$$

where $K_{CR}^{(1,2)}$ and $K_{I,CR}^{(1,2)}$ satisfy Eqs. (94) and (98), respectively. Moreover, $K_m^{(m)} = K_{I,p}^{(m)}$, meaning that $K_m^{(m)}$ is obtained from $K_p^{(m)}$ by applying the inverse gates in reversed order.

APPENDIX VI - ESTIMATION OF THE INFIDELITY USING INTERLEAVED RB

To estimate the infidelity $\bar{\varepsilon}$ associated with the CNOT gate, we follow Reference [34]. The Interleaved RB protocol is based on the original RB protocol used to estimate the average gate infidelity [9]. This is done by implementing random sequences of Clifford gates, which are followed by a final gate that inverts each sequence and generates the identity operation in the error-free case, and by measuring the probability to obtain the initial state $|0\rangle$. The sequence length l is the number of Clifford gates that compose it, including the gate that performs the reversion.

According to the RB theory [9], for a sequence of length l it holds that

$$F_l = A\alpha^l + B, \quad (113)$$

where F_l is the measured survival probability (probability of measuring $|0\rangle$), and α , A and B are constants to be experimentally determined. A and B account for SPAM errors, and α is used to estimate of the average gate infidelity. The average gate infidelity represents the infidelity averaged over Clifford gates as well as over the pure initial states. For n -qubit Clifford gates, this quantity is estimated in RB by

$$r_{\text{ave}} = \frac{2^n - 1}{2^n} (1 - \alpha). \quad (114)$$

The decay rate α is derived by fitting Eq. (113) to the experimental data points (l, F_l) , measured for different sequence lengths $1 \leq l \leq L$.

The Interleaved RB method combines this procedure with a similar protocol, where the random Clifford gates in a given sequence are interleaved with the (fixed) target gate. As in RB, the composition with the final gate must produce the identity operation in the absence of errors. Moreover, the sequence length is still defined as the number of random Clifford gates. The behavior of the corresponding survival probability can also be modeled using an exponential decay

$$\bar{F}_l = A\bar{\alpha}^l + B, \quad (115)$$

where \bar{F}_l is the survival probability for a sequence of length l . Therefore, the decay rate $\bar{\alpha}$ is obtained by fitting Eq. (115) to the experimental data (l, \bar{F}_l) . Using the parameters α and $\bar{\alpha}$, Interleaved RB yields the following estimate of the average infidelity for the target gate:

$$r = \frac{2^n - 1}{2^n} \left(1 - \frac{\bar{\alpha}}{\alpha}\right). \quad (116)$$

In our simulation, we consider sequence lengths such that $l = 3 + 15(k)$, with $0 \leq k \leq 20$. For each value of l , F_l and \bar{F}_l are survival probabilities averaged over 60 random Clifford sequences. We use the NonlinearModelFit function in the Mathematica software to derive the parameters α and $\bar{\alpha}$. The corresponding average infidelity r is evaluated for each value of the angles θ and ϕ , to obtain the orange curves in Fig. 2. NonlinearModelFit also allows us to compute errors $\Delta\alpha$ and $\Delta\bar{\alpha}$ associated with the quality of the fittings based on Eqs. (113) and (115). Using error propagation, the error bars for the orange curves are evaluated as

$$\Delta r = \frac{2^n - 1}{2^n} \sqrt{\frac{\bar{\alpha}^2(\Delta\alpha)^2 + \alpha^2(\Delta\bar{\alpha})^2}{\alpha^4}}. \quad (117)$$

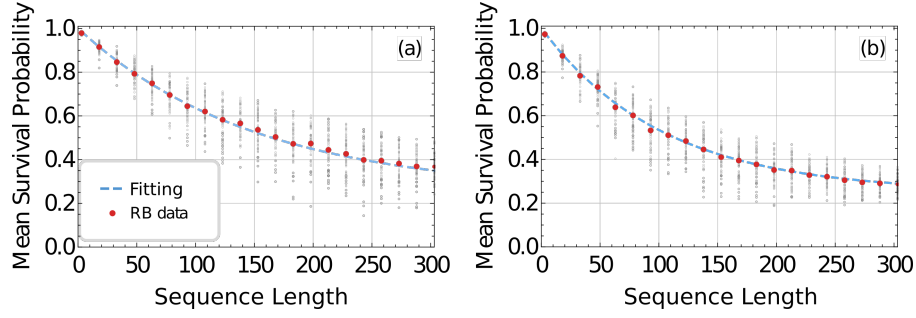


Figure 3. Interleaved RB simulations for the estimate of the (CNOT) gate infidelity corresponding to $\theta = 0.05$, $\phi = 0.04$, and $\xi = 0.001$. (a) The RB data (red dots) for the survival probability averaged over random sequences of Clifford gates. For each sequence length the average is taken over 60 samples (gray dots). The dashed blue curve gives the fit according to Eq. (113). (b) Interleaved RB data (red dots) and fit (115) (dashed blue curve). In this case the 60 random sequences per each sequence length contain Clifford gates interleaved with the CNOT gate.

In Fig. 3, we show the RB and Interleaved RB simulations corresponding to Eqs. (113) and (115), respectively. These simulations are performed for $\theta = 0.05$, $\phi = 0.04$, and $\xi = 0.001$. The red dots are the averages F_l and \bar{F}_l (taken over the data depicted by the gray dots), and the dashed blue curves are the fitting curves. Importantly, all the errors sources described in Appendix V are included in these simulations. Figure 3 shows the good quality of the fits corresponding to the aforementioned parameters, which we also corroborated with the simulations using other error parameters. This evidences that, in our example, the substantial disparity between the curves for r and $\bar{\varepsilon}$ in Fig. 2 is a consequence of the inability of Interleaved RB to predict the actual average infidelity.

APPENDIX VII - DERIVATION OF THE BOUNDS (49) AND (50)

To obtain the bounds (49) and (50), we express the solutions to Eqs. (53) and (62) using the Dyson series. For Eq. (53), we have that

$$e^{\Omega(T)} = \sum_{k=0}^{\infty} \frac{1}{k!} \int_0^T dt_1 \int_0^T dt_2 \dots \int_0^T dt_k \mathcal{T} \mathcal{L}^{int}(t_1) \mathcal{L}^{int}(t_2) \dots \mathcal{L}^{int}(t_k), \quad (118)$$

where \mathcal{T} is the time ordering operator. The first and second terms in the Dyson expansion (118) are I_L and Ω_1 , respectively. Therefore,

$$\begin{aligned} |\varepsilon_{\text{inc}}(\varrho, \tilde{\sigma}) + \langle \Omega_1 \rangle| &= \left| \langle \langle \rho_0 | I_L - e^{\Omega(T)} + \Omega_1 | \rho_0 \rangle \rangle \right| \\ &\leq \left\| I_L - e^{\Omega(T)} + \Omega_1 \right\| \\ &= \left\| \sum_{k=2}^{\infty} \frac{1}{k!} \int_0^T dt_1 \int_0^T dt_2 \dots \int_0^T dt_k \mathcal{T} \mathcal{L}^{int}(t_1) \dots \mathcal{L}^{int}(t_k) \right\| \\ &\leq \sum_{k=2}^{\infty} \frac{1}{k!} \left(\int_0^T dt \|\mathcal{L}^{int}(t)\| \right)^k \\ &= \sum_{k=2}^{\infty} \frac{1}{k!} \left(\int_0^T dt \|\mathcal{L}(t)\| \right)^k, \end{aligned} \quad (119)$$

where $\|\cdot\|$ stands for the spectral norm. The second line of Eq. (119) follows from the definition of the spectral norm (and the fact that $\langle \langle \rho_0 | \rho_0 \rangle \rangle = 1$), and the fourth line is a consequence of the submultiplicativity of $\|\cdot\|$ and the triangle inequality. In the last line we apply the unitary invariance of this norm. Writing $\sum_{k=2}^{\infty} \frac{1}{k!} \left(\int_0^T dt \|\mathcal{L}(t)\| \right)^k$ as $e^{\int_0^T dt \|\mathcal{L}(t)\|} - 1 - \int_0^T dt \|\mathcal{L}(t)\|$, we obtain Eq. (49).

Let us now derive the bound (50). We express the difference $e^{\Omega(2T)} - e^\chi$ as $e^{\Omega(2T)} - e^\chi = (e^{\Omega(2T)} - I_L - \chi) - \sum_{k=2}^{\infty} \frac{1}{k!} \chi^k$, and apply the triangle inequality to obtain

$$\left\| e^{\Omega(2T)} - e^\chi \right\| \leq \left\| e^{\Omega(2T)} - I_L - \chi \right\| + \sum_{k=2}^{\infty} \frac{1}{k!} \|\chi\|^k. \quad (120)$$

Now, keeping in mind that $\chi = \Omega_1(2T)$, the term $\|e^{\Omega(2T)} - I_L - \chi\|$ is analogous to $\|I_L - e^{\Omega(T)} + \Omega_1\|$ in the second line of Eq. (119). Specifically, in both cases we have the subtraction between the exact evolution and the sum of the corresponding first Magnus term plus I_L . As a consequence, the application of the Dyson expansion

$$e^{\Omega(2T)} = \sum_{k=0}^{\infty} \frac{1}{k!} \int_0^{2T} dt_1 \int_0^{2T} dt_2 \dots \int_0^{2T} dt_k \mathcal{T} (\mathcal{L}'_{\text{ext}})^{\text{int}}(t_1) \dots (\mathcal{L}'_{\text{ext}})^{\text{int}}(t_k), \quad (121)$$

and the same steps followed in Eq. (119), lead to

$$\begin{aligned} \left\| e^{\Omega(2T)} - I_L - \chi \right\| &\leq \sum_{k=2}^{\infty} \frac{1}{k!} \left(\int_0^{2T} dt \|\mathcal{L}'_{\text{ext}}(t)\| \right)^k \\ &= e^{\int_0^{2T} dt \|\mathcal{L}'_{\text{ext}}(t)\|} - 1 - \int_0^{2T} dt \|\mathcal{L}'_{\text{ext}}(t)\|. \end{aligned} \quad (122)$$

Since $\mathcal{L}'_{\text{ext}} = \mathcal{L}_{\text{ext}}(t) - i\delta H_L(t)$ (cf. Eqs. (48) and (60)), Eq. (122) yields half of the bound (50). The other half results from the series $\sum_{k=2}^{\infty} \frac{1}{k!} \|\chi\|^k$. By expressing $\chi = \Omega_1(2T)$ as in Eq. (64), it follows that

$$\begin{aligned} \sum_{k=2}^{\infty} \frac{1}{k!} \|\chi\|^k &= \sum_{k=2}^{\infty} \frac{1}{k!} \left\| \int_0^{2T} dt (\mathcal{L}'_{\text{ext}})^{\text{int}}(t) \right\|^k \\ &\leq \sum_{k=2}^{\infty} \frac{1}{k!} \left(\int_0^{2T} dt \|\mathcal{L}'_{\text{ext}}(t)\| \right)^k \\ &= e^{\int_0^{2T} dt \|\mathcal{L}'_{\text{ext}}(t)\|} - 1 - \int_0^{2T} dt \|\mathcal{L}'_{\text{ext}}(t)\|. \end{aligned} \quad (123)$$

Therefore, $\|e^{\Omega(2T)} - e^\chi\|$ in (120) is bounded by

$$\begin{aligned} \left\| e^{\Omega(2T)} - e^\chi \right\| &\leq 2 \left(e^{\int_0^{2T} dt \|\mathcal{L}'_{\text{ext}}(t)\|} - \int_0^{2T} dt \|\mathcal{L}'_{\text{ext}}(t)\| - 1 \right) \\ &= 2 \left(e^{\int_0^{2T} dt \|\mathcal{L}_{\text{ext}}(t) - i\delta H_L(t)\|} - \int_0^{2T} dt \|\mathcal{L}_{\text{ext}}(t) - i\delta H_L(t)\| - 1 \right). \end{aligned} \quad (124)$$